Aspects of Pulsar Navigation for Deep Space Mission Applications

Po-Ting Chen[1] · Bonan Zhou[1] · Jason L. Speyer[1] · David S. Bayard[2] · Walid A. Majid[2] · Lincoln J. Wood[2]

Abstract

This paper investigates the performance of pulsar-based navigation in deep space mission applications. The noise properties of X-ray based and radio-baspulsar measurements are examined and compared. A closed form parametric covariance analysis tool was developed in this study. It provides a rough estimate of the navigation performance associated with a deep space cruise that makes use of ion thrusters and sequential pulsar observations. In addition, the flight trajectory of the Dawn spacecraft was used to form a hypothetical deep space mission scenario that utilizes pulsars as navigation beacons. This simulated scenario accounts for clock uncertainty, pulsar timing noise, maneuver execution errors, sequential observation and interruptions between pulsar observations. A particle filter was implemented to reduce the large initial position uncertainty by resolving the number of pulsar wavelengths between the spacecraft and the Solar System Barycenter. The resulting position and velocity uncertainties from the particle filter can be used to initialize an Extended Kalman Filter, which estimates the spacecraft position and velocity for steady state operations.

Keywords Pulsar · Navigation · Integer ambiguity resolution · Covariance analysis

✉ Po-Ting Chen
p7chen@ucla.edu

Jason L. Speyer
speyer@g.ucla.edu

1 Mechanical and Aerospace Engineering Department, University of California Los Angeles, Los Angeles, CA 90095, USA

2 Jet Propulsion Laboratory, California Institute of Technology, Pasadena, CA 91109, USA

Introduction

Space exploration has been an integral part of modern human history. As we explore further into deep space, technological advancements are necessary to continue this journey. Certain deep space missions can be enabled or enhanced with the use of an autonomous navigation system. One novel approach is observing and processing signals from rapidly rotating and highly magnetized neutron stars, called pulsars [19]. These celestial objects rotate about an axis just like Earth, but as they rotate charged particles along the magnetic field lines are accelerated to generate electromagnetic radiation. This beam of energy consists of components across the entire electromagnetic spectrum. Because of the misalignment between the pulsar's rotational and magnetic axes, the energy beam sweeps across the sky as the pulsar rotates. The detection of the beam is only possible when the emission direction is aligned with the line-of-sight of an observer. From the perspective of the observer, a pulsar signal is analogous to the beacon of a distant lighthouse. The rotation periods range from 8.5 s to 1.39 ms, which translate to wavelengths between 2.5×10^6 km and 419 km. While these numbers seem large, they are minuscule comparing to the size of the Solar System. The mean distance between Pluto and the Sun is approximately 40 AU, where one Astronomical Unit (AU) is approximately 1.50×10^8 km.

There have been multiple studies in pulsar-based navigation since the discovery of pulsars in 1967. This navigation concept relies on determining the number of pulsar signal wavelengths between a spacecraft and the Solar System Barycenter (SSB) [3, 24, 28, 29]. Due to the exceptional stability of the pulsing behavior, the phase of this periodic signal can be tracked to determine the position and the velocity of the spacecraft relative to the SSB. Most pulsar-based navigation techniques rely on a two-stage approach. The first stage is a signal estimator based on parameter estimation methods such as cross-correlation, nonlinear least squares, or Maximum Likelihood Estimation (MLE). The purpose of this step is to obtain estimates of the pulsar signal phase offset and/or Doppler frequency from raw waveform measurements [10, 12]. These two estimates contain information about the spacecraft position and velocity relative to the SSB. The second stage relies on a Kalman-type nonlinear filter to recursively process the outputs of the signal estimator together with a dynamical model to generate a state estimate [10, 18, 30, 33]. The NASA Neutron star Interior Composition ExploreR (NICER) mission and the Station Explorer X-ray Timing And Navigation Technology (SEXTANT) mission implement a refined version of the MLE that uses the *a priori* mean of the spacecraft states to predict the signal phase in order to compensate for extended observation duration [34, 35]. When there are significant correlated noises embedded in the pulsar measurements, a more coherent approach is to directly process the raw waveform measurements with a Kalman-type nonlinear filter [7]. In 2018, X-ray pulsar-based navigation was demonstrated by the NICER/SEXTANT team and achieved an accuracy of $\sim$ 10 km after processing the pulsar measurements on the International Space Station for 1 day [21].

Building on the above research, this paper investigates the performance of pulsar-based spacecraft navigation using a Design Reference Mission (DRM). The trajectory of the Dawn spacecraft was chosen for this study. The purpose of using a DRM is to consider a realistic deep space mission scenario that could make use of sequential

pulsar observation. Section "Design Reference Mission" and "Pulsar Model" discuss the DRM, spacecraft dynamics and pulsar model. Section "Navigation System" shows the state space model for the numerical simulation. A covariance analysis is included in "Covariance Analysis". Section "Particle Filter for Position Acquisition" discusses the use of particle filter to reduce the large initial position uncertainty in which the integer ambiguity in the number of pulsar wavelengths from the spacecraft to the SSB was resolved. Section "Extended Kalman Filter for Steady State Operations" shows the subsequent nominal navigation performance from an Extended Kalman Filter (EKF).

Design Reference Mission

NASA launched the Dawn spacecraft in September 2007. Its mission was to travel to the asteroid belt using ion propulsion and to survey the two large asteroids Vesta and Ceres. Figure 1 shows the mission timeline from launch to completion. This spacecraft is equipped with three ion thrusters developed using proven technologies from
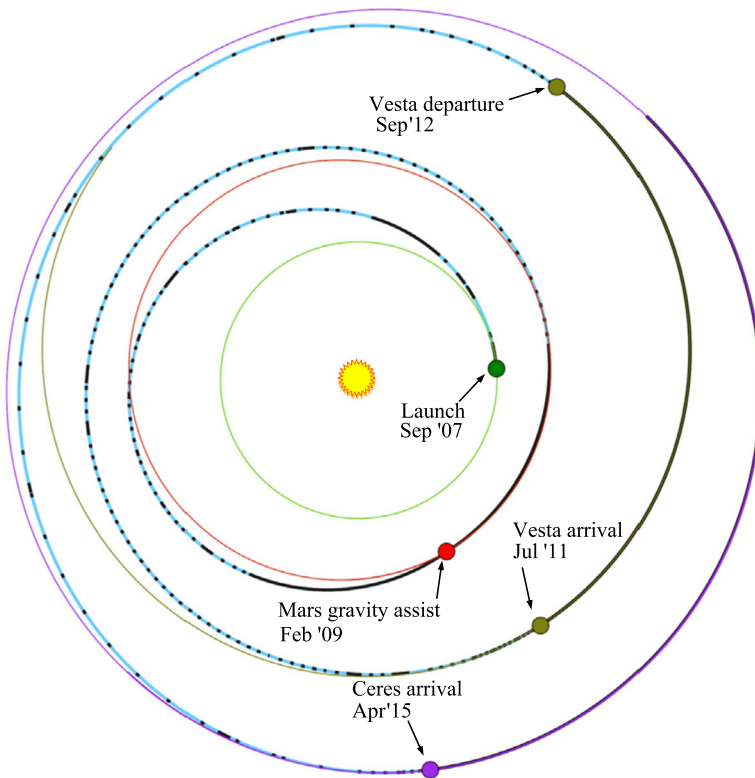

Fig. 1 Complete mission trajectory. The blue trajectory corresponds to the thrusting segment, and the black trajectory is the coasting segment [25]

the Deep Space 1 mission. These thrusters enable Dawn to travel to and enter into orbit around Vesta and Ceres. After deploying its solar panels, Dawn has a wingspan of 19.7 m. The total mass of the spacecraft at the start of the mission is 1217 kg, which consists of a 747 kg spacecraft mass, 425 kg of xenon propellant and 46 kg of hydrazine propellant [27]. As indicated by Fig. 1, the spacecraft went through multiple coasting and thrusting segments.

The Dawn ephemeris file has 11 columns of data: XYZ position, XYZ velocity, XYZ thrust, time, and spacecraft mass. The starting date is 2454385 JED and the terminal date is 2455759 JED, where JED is Julian Ephemeris Day. The first date is approximately 2 weeks after the launch of the spacecraft and the second date corresponds to the time of arrival at Vesta. The 3-dimensional trajectory from the ephemeris is plotted in Fig. 2, where the red star is the Sun. The red triangle is the start of the ephemeris file. The kink in the trajectory followed by a change in orbital inclination corresponds to the gravity assist at Mars on Feb. 17, 2009 (2454879.5 JED). The inclination change is exaggerated by the stretching of the Z-axis.

Spacecraft Dynamics

In order to use the ephemeris for the study while simplifying the dynamical model of the spacecraft, the following approximation was used. It was assumed that the spacecraft acceleration could be approximately modeled as

$$\ddot{\boldsymbol{r}}_{sc}(t) = -\frac{\mathcal{G}m_\odot}{\|\boldsymbol{r}_{sc}(t)\|^3}\boldsymbol{r}_{sc}(t) + \boldsymbol{d}(t) + \boldsymbol{u}(t), \tag{1}$$

where $\mathcal{G}$ is the gravitational constant; $m_\odot$ is the mass of the Sun; $\boldsymbol{r}_{sc}(t)$ is the spacecraft position relative to the Sun; $\boldsymbol{d}(t)$ is an unknown residual acceleration; and $\boldsymbol{u}(t)$
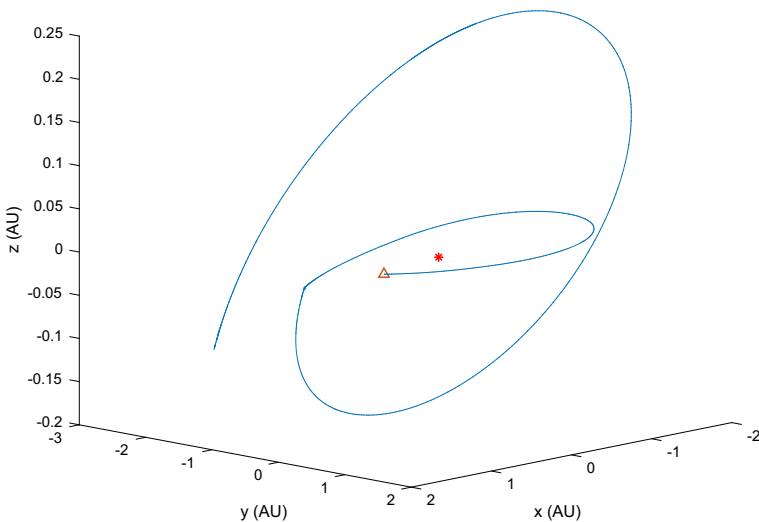

Fig. 2 3-dimensional heliocentric trajectory of the Dawn spacecraft from Earth to Vesta

is the commanded acceleration from the ion thrusters. Since the velocity of the spacecraft, $\dot{\boldsymbol{r}}_{sc}(t)$, is provided in the ephemeris file, a numerical finite difference method was used to determine the approximate value for the left hand side of Eq. 1 denoted as $\ddot{\boldsymbol{r}}_{sc}^{fd}(t)$. Therefore, the unknown acceleration can be determined by solving Eq. 1 for $\boldsymbol{d}(t)$ and substituting in the finite differenced accelerations,

$$\boldsymbol{d}(t) = \ddot{\boldsymbol{r}}_{sc}^{fd}(t) + \frac{\mathcal{G}m_{\odot}}{\|\boldsymbol{r}_{sc}(t)\|^3}\boldsymbol{r}_{sc}(t) - \boldsymbol{u}(t). \tag{2}$$

This residual acceleration is treated as a deterministic term in numerical simulation and filter design. Figure 3 shows the duration of the thrusting and coasting segments of the ephemeris in the top plot. The magnitude of $\boldsymbol{u}(t)$ is plotted in the middle plot and the last plot shows the magnitude of $\boldsymbol{d}(t)$. The large spike at around day 500 in the last plot is the Mars gravity assist. From the top plot, the typical coasting segment is between 7 to 8 hours and the thrusting segment is between 6 to 7 days. If the pulsar-based navigation system is only allowed to observe pulsars during coasting segments, then the available observation time is approximately 5% of the total cruise time from Earth to Vesta.

In addition to the above deterministic model, two stochastic acceleration disturbances are added. The first is $\boldsymbol{w}_r(t)$, which is a white noise disturbance with a
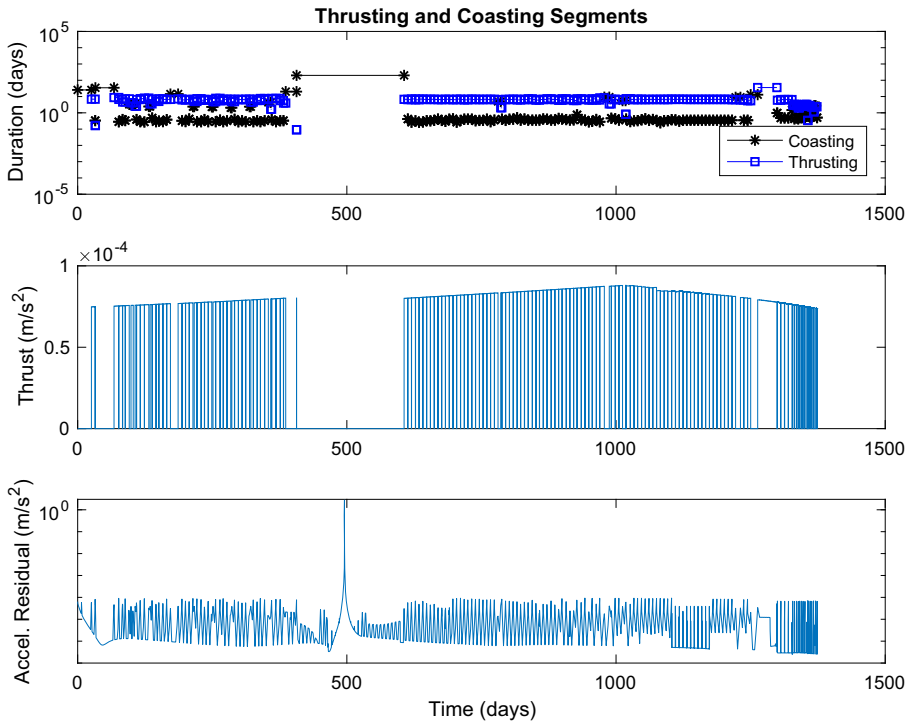

Fig. 3 Thrusting and coasting schedule

constant Power Spectral Density (PSD) of W_r. The second disturbance, $\boldsymbol{w}_g(t)$, is also white and is a result of using the ion thrusters. In other words, if $\|\boldsymbol{u}(t)\| = 0$, then $\boldsymbol{w}_g(t) = 0$. The first component of $\boldsymbol{w}_g(t)$ is the disturbance along the thrusting direction and the two other components correspond to disturbances normal to the thrusting direction. All three components are uncorrelated with each other. The PSD of this disturbance is denoted as $W_g(t)$ and it is set following the Gates model [11],

$$[W_g(t)]_{ii} = \frac{(\sigma_{fixed,i}\Delta t)^2 + (\sigma_{prop,i}\Delta V(t))^2}{\Delta t}, \tag{3}$$

where $i = 1, 2, 3$; $\Delta V(t) = \|\boldsymbol{u}(t)\|\Delta t$; and Δt is the integration time step. The symbol $[A]_{ij}$, means the ith row and j^{th} component of the A matrix. If A is a vector, then only the ith index is provided. The Gates method separates the acceleration disturbance into a fixed part, $\sigma_{fixed,i}$, and a proportional part, $\sigma_{prop,i}$. The coefficient, $\sigma_{fixed,i}$, models disturbances that are independent of the magnitude of the commanded acceleration in the ith direction. The coefficient, $\sigma_{prop,i}$, models disturbances that are proportional to the magnitude of the commanded acceleration. Adding $\boldsymbol{w}_r(t)$ and $\boldsymbol{w}_g(t)$ to Eq. 1 gives

$$\ddot{\boldsymbol{r}}_{sc}(t) = -\frac{Gm_\odot}{\|\boldsymbol{r}_{sc}(t)\|^3}\boldsymbol{r}_{sc}(t) + \boldsymbol{d}(t) + \boldsymbol{u}(t) + \boldsymbol{w}_r(t) + G_g(t)\boldsymbol{w}_g(t), \tag{4}$$

where $G_g(t)$ is a transformation matrix from the thruster frame to the inertial frame,

$$G_g(t) = \begin{bmatrix} \cos(\alpha) & -\sin(\alpha) & 0 \\ \sin(\alpha) & \cos(\alpha) & 0 \\ 0 & 0 & 1 \end{bmatrix} \begin{bmatrix} \cos(\beta) & 0 & \sin(\beta) \\ 0 & 1 & 0 \\ -\sin(\beta) & 0 & \cos(\beta) \end{bmatrix}$$

$$\alpha(t) = \operatorname{atan2}\left([\hat{\boldsymbol{u}}(t)]_2, [\hat{\boldsymbol{u}}(t)]_1\right)$$

$$\beta(t) = -\operatorname{atan2}\left([\hat{\boldsymbol{u}}(t)]_3, \sqrt{[\hat{\boldsymbol{u}}(t)]_1^2 + [\hat{\boldsymbol{u}}(t)]_2^2}\right)$$

$$\hat{\boldsymbol{u}}(t) = \frac{\boldsymbol{u}(t)}{\|\boldsymbol{u}(t)\|}. \tag{5}$$

The thruster frame is defined such that the X-axis ($i = 1$) corresponds to the thrusting direction.

Pulsar Model

The phase (rotation) evaluation of a millisecond pulsar is

$$\phi\left(t^{psr}\right) = \phi_0 + \dot{\phi}\left[t^{psr} - t_0\right] + \frac{1}{2}\ddot{\phi}\left[t^{psr} - t_0\right]^2, \tag{6}$$

where ϕ_0, $\dot{\phi}$, $\ddot{\phi}$, and t_0 are all known values obtained from prior observations [9]. The time t^{psr} is the signal emission time at the pulsar center of mass. The electromagnetic intensity measurement at the spacecraft is modeled as

$$y(t^{sc}) = \lambda_b + \lambda_s s\left(\phi_{sc}(t^{sc})\right) + \upsilon(t^{sc}), \tag{7}$$

where λ_b is the background strength and λ_s is the source strength. The time t^{sc} is the measurement time at the spacecraft. The function $s(\cdot)$ is periodic and normalized such that

$$\int_0^1 s(\phi)\, d\phi = 1. \tag{8}$$

$s(\cdot)$ describes the pulsar signal profile and is unique to each pulsar. The phase equation $\phi_{sc}(t^{sc})$ is a time shifted version of $\phi(t^{psr})$ [9]. The amount of time shift is described by a system of time transfer equations,

$$
\begin{aligned}
t^{ssb} &= t^{sc} - \Delta_\odot \left(t^{sc}, t^{bb}, \boldsymbol{r}(t^{sc}) \right) \\
t^{bb} &= t^{ssb} - \Delta_{IS} \left(t^{ssb}, t^{bb}, \boldsymbol{r}(t^{sc}) \right) \\
t^{psr} &= t^{bb} - \Delta_B \left(t^{bb}, t^{psr}, \boldsymbol{r}(t^{sc}) \right),
\end{aligned}
\tag{9}
$$

where t^{ssb} and t^{bb} are the time of arrival of the pulsar signal at the SSB and the pulsar binary barycenter respectively. The position of the spacecraft relative to the SSB is $\boldsymbol{r}$. $\Delta_\odot$, Δ_{IS}, and Δ_B represent the Solar System, interstellar, and binary delays respectively. Solving Eq. 9 for t^{psr} requires the Solar System and time ephemerides [15, 22]. Of all the delay terms in Eq. 9, the dominant term is the Roemer delay,

$$\Delta_{R\odot} = -\frac{\boldsymbol{n}^T \boldsymbol{r}}{c}, \tag{10}$$

embedded in the Solar System delay, $\Delta_\odot$, where $\boldsymbol{n}$ is the pulsar direction unit vector expressed in the inertial frame located at the SSB. $\Delta_{R\odot}$ accounts for the geometric delay due to light travel time as illustrated in Fig. 4.

In order to limit the scope of the study, only the signal frequency, $\dot{\phi}$, and the Roemer delay, $\Delta_{R\odot}$, are modeled. The reasoning for the simplification is that the frequency rate, $\ddot{\phi}$, and the rest of the time transfer terms are much smaller than the
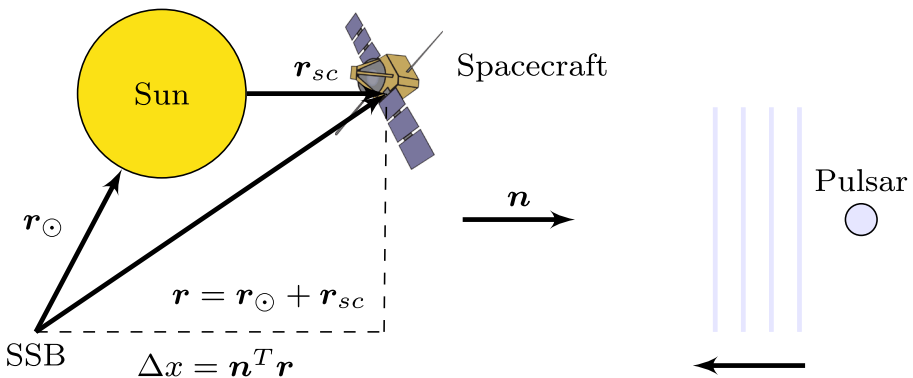

Fig. 4 The spacecraft is in orbit around the Sun. The unit vector, $\boldsymbol{n}$, points toward the pulsar and $\boldsymbol{r}_\odot$ is the Sun position vector relative to the SSB. $\boldsymbol{r}_\odot$ is exaggerated in this figure

frequency and the Roemer delay respectively [13]. The simplified time transfer for this study is

$$t^{psr} = t^{sc} + \frac{\boldsymbol{n}^T \boldsymbol{r}(t^{sc})}{c}. \tag{11}$$

It is worth pointing out that the particle filter in "Particle Filter for Position Acquisition" and the EKF in "Extended Kalman Filter for Steady State Operations" can accommodate the general time transfer in Eq. 9.

Substituting Eq. 11 into Eq. 6 and neglecting $\ddot{\phi}$ gives the phase equation at the spacecraft,

$$\phi_{sc}(t^{sc}) = \phi_0 + \dot{\phi}\left[t^{sc} + \frac{\boldsymbol{n}^T \boldsymbol{r}_{sc}(t^{sc})}{c} + t_c(t^{sc}) - t_0\right] + n_\zeta(t^{sc}), \tag{12}$$

where t_c and n_ζ are added to account for clock noise and the pulsar timing noise. The uncertainty in $\boldsymbol{r}_\odot$ is assumed to be smaller than the positioning accuracy of pulsar-based navigation, so it is not modeled in this study. For the purpose of clarity, the superscript sc is neglected in the rest of the paper.

Radio Frequency

The statistical properties of the measurement noise, $v(t)$, depend on the pulsar observation frequency. If radio pulsars are used, then a Gaussian process is used to model the measurement of the signal waveform. The background source strength and signal strength are

$$\lambda_{b,rf} = T_{sys} \quad \text{and} \quad \lambda_{s,rf} = \tilde{\lambda}_{s,rf} G_{rf}, \tag{13}$$

where $\tilde{\lambda}_{s,rf}$ is the source flux density in Janskys (Jy). The units of $\lambda_{b,rf}$ and $\lambda_{s,rf}$ are Kelvins (K). The antenna gain and antenna area are

$$G_{rf} = \frac{A_{rf}\eta_{rf}}{2k_B} \quad \text{and} \quad A_{rf} = \frac{\pi d_{rf}^2}{4}, \tag{14}$$

where d_{rf} is the antenna diameter; η_{rf} is the antenna efficiency; and k_B is the Boltzmann constant. The gain represents the sensitivity of an antenna to a radio source. The measurement noise PSD, V_{rf}, is given by the radiometer equation,

$$V_{rf} = \frac{T_{sys}^2}{n_p \Delta f}, \tag{15}$$

where T_{sys} is the system noise temperature; Δf is the system bandwidth; n_p is the number of polarizations [19]. The system temperature is a sum of receiver noise temperature, spillover noise temperature, and sky background noise temperature. Unlike the X-ray measurement in "X-Ray Frequency", the noise due to sky background is independent of the antenna size [5]. The mean and variance of the measurement noise is

$$E[v(t)] = 0, \text{ and } \mathrm{var}[v(t)] = \frac{V_{rf}}{\Delta t}, \tag{16}$$

where Δt is the sampling interval [32].

X-Ray Frequency

If X-ray pulsars are used as navigation beacons, then a non-homogenous Poisson process is used to model the detection of individual X-ray photons [10]. The rates of the process are

$$\lambda_{b,xr} = \tilde{\lambda}_{b,xr} A_{xr} \eta_{xr}, \quad \lambda_{s,xr} = \tilde{\lambda}_{s,xr} A_{xr} \eta_{xr}, \tag{17}$$

where

$$A_{xr} = \frac{\pi d_{xr}^2}{4}. \tag{18}$$

η_{xr} is the area efficiency factor; A_{xr} is the detector geometric frontal area; and d_{xr} is the detector diameter. The units of $\lambda_{b,xr}$ and $\lambda_{s,xr}$ are photons per second (ph/s). The statistics of the measurement noise are

$$E[v(t)] = 0, \text{ and } \mathrm{var}[v(t)] = \frac{\lambda_{b,xr} + \lambda_{s,xr} s_{xr}(\phi_{sc}(t))}{\Delta t}. \tag{19}$$

Because of the form of Eq. 19, one can interpret the non-homogenous Poisson process as having a periodic PSD, $V_{xr}(t) = \lambda_{b,xr} + \lambda_{s,xr} s_{xr}(\phi_{sc}(t))$.

Timing Noise

While millisecond pulsars have stable rotational dynamics, they are still corrupted by a small amount of fractional stationary noise whose PSD is

$$S_{n_\zeta}(\omega) = \frac{W_\zeta}{\left(1 + \left(\frac{\omega}{\omega_c}\right)^2\right)^\alpha}, \tag{20}$$

where w_ζ, α, and ω_c are positive fitting parameters [8]. They represent the strength of the white noise, the integration order, and the corner frequency of a fractional Linear Time Invariant (LTI) system. The parameters of Eq. 20 for various pulsars can be found in the current literature [26]. The typical value of ω_c is between 3 rad/yr and 0.4 rad/yr, which translates to a time constant between 0.33 yr to 2.5 yr. Eqution 20 is termed fractional because the parameter α is not necessary an integer value. The typical value for α is between 1 and 3. The fractional PSD in Eq. 20 can be approximated over a bandwidth by interweaving zeros and poles [6]. The approximated system is essentially a high-order stable LTI system. Therefore, the pulsar timing noise in this study is modeled using a shaping filter with a large time constant,

$$\begin{aligned} \dot{\zeta}(t) &= F_\zeta \zeta(t) + G_\zeta w_\zeta(t) \\ n_\zeta(t) &= H_\zeta \zeta(t) \end{aligned} \tag{21}$$

where F_ζ is a stable matrix.

Navigation System

We assume the spacecraft carries a clock whose error model is

$$\begin{bmatrix} \dot{t}_c(t) \\ \dot{b}_c(t) \end{bmatrix} = \underbrace{\begin{bmatrix} 0 & 1 \\ 0 & 0 \end{bmatrix}}_{F_c} \underbrace{\begin{bmatrix} t_c(t) \\ b_c(t) \end{bmatrix}}_{t_c} + \underbrace{\begin{bmatrix} 1 & 0 \\ 0 & 1 \end{bmatrix}}_{G_c} w_c(t)$$

$$t_c(t) = \underbrace{\begin{bmatrix} 1 & 0 \end{bmatrix}}_{H_c} \begin{bmatrix} t_c(t) \\ b_c(t) \end{bmatrix}, \tag{22}$$

where $t_c(t)$ is the clock bias and $b_c(t)$ is the clock drift [4]. Combining Eq. 4 with Eqs. 7, 21 and 22 gives the state space model for numerical simulation,

$$\begin{bmatrix} \dot{r}_{sc}(t) \\ \ddot{r}_{sc}(t) \\ \dot{t}_c(t) \\ \dot{\zeta}_p(t) \end{bmatrix} = \begin{bmatrix} 0 & I_{3x3} & 0 & 0 \\ -\frac{Gm_\odot}{\|r_{sc}(t)\|^3} I_{3x3} & 0 & 0 & 0 \\ 0 & 0 & F_c & 0 \\ 0 & 0 & 0 & F_{\zeta,p} \end{bmatrix} \begin{bmatrix} r_{sc}(t) \\ \dot{r}_{sc}(t) \\ t_c(t) \\ \zeta_p(t) \end{bmatrix}$$

$$+ \begin{bmatrix} 0 \\ d(t) + u(t) \\ 0 \\ 0 \end{bmatrix} + \begin{bmatrix} 0 & 0 & 0 & 0 \\ I & G_g(t) & 0 & 0 \\ 0 & 0 & G_c & 0 \\ 0 & 0 & 0 & G_{\zeta,p} \end{bmatrix} \begin{bmatrix} w_r(t) \\ w_g(t) \\ w_c(t) \\ w_{\zeta,p}(t) \end{bmatrix}$$

$$y_p(t_j) = \lambda_{b,p} + \lambda_{s,p} s_p(\phi_{sc,p}(t_j)) + v_p(t_j). \tag{23}$$

The subscript p is added to ζ and y to indicate the timing noise and the intensity measurement of the pth pulsar. It ranges from 1 to N_{pulsar}, where N_{pulsar} is the number of observed pulsars. The phase equation at the spacecraft is

$$\phi_{sc,p}(t_j) = \phi_{0,p} + \dot{\phi}_p \left[t_j - t_0 + \underbrace{\frac{n_p^T r_{sc}(t_j)}{c}}_{\text{geometric delay}} + \underbrace{H_c t_c(t_j)}_{\text{clock noise}} \right] + \underbrace{H_{\zeta,p} \zeta_p(t_j)}_{\text{pulsar timing noise}} \tag{24}$$

The measurement noise variance is given by Eq. 19. This navigation system is formulated using continuous time dynamics and discrete time measurements. The sample time is given by t_j. The measurement is $y_p(t_j)$ and the state vector is

$$x(t) = \begin{bmatrix} r_{sc}(t) & \dot{r}_{sc}(t) & t_c(t) & \zeta_p(t) \end{bmatrix}^T. \tag{25}$$

The time correlations of the process noises are

$$E[w_r(t)w_r^T(\tau)] = W_r \delta(t - \tau)$$
$$E[w_g(t)w_g^T(\tau)] = W_g(t)\delta(t - \tau)$$
$$E[w_c(t)w_c^T(\tau)] = W_c \delta(t - \tau)$$
$$E[w_{\zeta,p}(t)w_{\zeta,p}^T(\tau)] = W_{\zeta,p} \delta(t - \tau). \tag{26}$$

Covariance Analysis

As shown in Eq. 23, the navigation problem has nonlinear dynamics and nonlinear measurements. The measurement function is given in terms of pulsar parameters such as frequency, direction, intensity and waveform profile. The measurement noise variance is also related to the pulsar parameters. Because of the nonlinearity, the impact of individual pulsar parameters on the overall navigation accuracy is not obvious. Therefore, this section uses linearized covariance analysis to develop an intuitive understanding.

X-ray Based vs. Radio Based Pulsar Timing System

This section investigates the timing accuracy of an X-ray based system and a radio-based system. Let the timing accuracy of the X-ray based system due to photon noise (a non-homogenous Poisson process) and that of the radio-based system due to radiometer noise (a Gaussian process) be defined as σ_{xr}^2 and σ_{rf}^2 respectively. For the X-ray based system, the uncertainty is quantified using the Cramér-Rao Lower Bound (CRLB) [10],

$$\sigma_{xr}^2 = \frac{1}{\lambda_{s,xr}^2 T_{obs} \dot{\phi}^2} \left[\int_0^1 \frac{s_{xr}'(\varphi)^2}{\lambda_{b,xr} + \lambda_{s,xr} s_{xr}(\varphi)} d\varphi \right]^{-1}, \qquad (27)$$

where the prime symbol denotes the derivative with respect to the argument of the function. The parameter T_{obs} is the observation time; $\dot{\phi}$ is the pulsar frequency; $\lambda_{b,xr}$ and $\lambda_{s,xr}$ are the background and source rates given in Eq. 17.

On the other hand, the timing uncertainty of the radio-based system is obtained using the covariance analysis result in [7],

$$\sigma_{rf}^2 = \frac{V_{rf}}{2\pi^2 \lambda_{s,rf}^2 T_{obs} \dot{\phi}^2} \left[\sum_{j=1}^{N_f} j^2 \left(a_j^2 + b_j^2 \right) \right]^{-1}, \qquad (28)$$

where $\lambda_{s,rf}$ is the signal temperature given by Eq. 13; V_{rf} is the PSD of the noise given by Eq. 15; a_j and b_j are the Fourier coefficients describing the signal profile; and N_f is the number of Fourier series terms used. It is worth pointing out that Eq. 28 is consistent with the approximate timing accuracy formula,

$$
\begin{aligned}
\sigma_{rf,w}^2 &= \frac{V_{rf}}{\lambda_{s,rf}^2 T_{obs}} \left[\frac{W^3}{4(P-W)} \right] \\
&= \frac{V_{rf}}{\lambda_{s,rf}^2 T_{obs} \dot{\phi}^2} \left[\frac{\gamma^3}{4(1-\gamma)} \right],
\end{aligned} \qquad (29)
$$

which is derived using the profile pulse width [2]. $P = 1/\dot{\phi}$ is the pulsar signal period; W is the full width at half maximum of a Gaussian approximation of the pulse profile; and $\gamma = W/P$ is the pulse fraction.
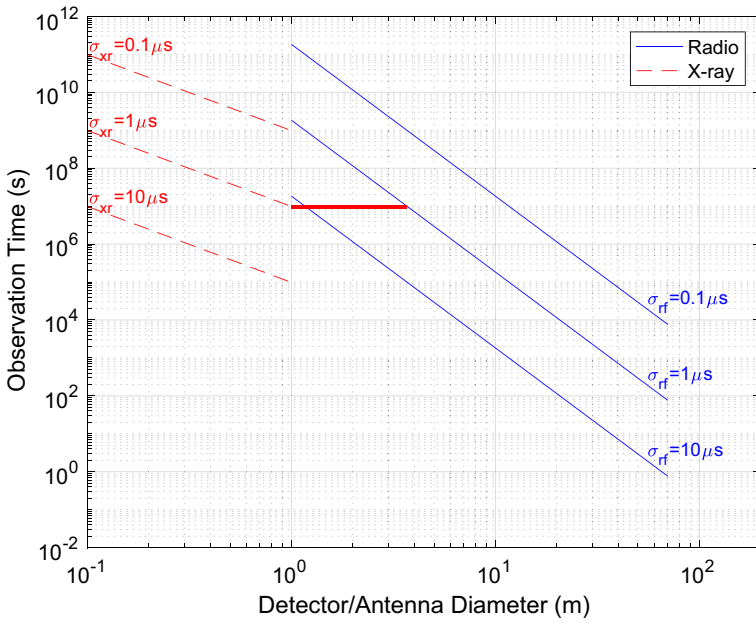
Fig. 5 Required observation time for a given timing accuracy and detector size for J0437-4715
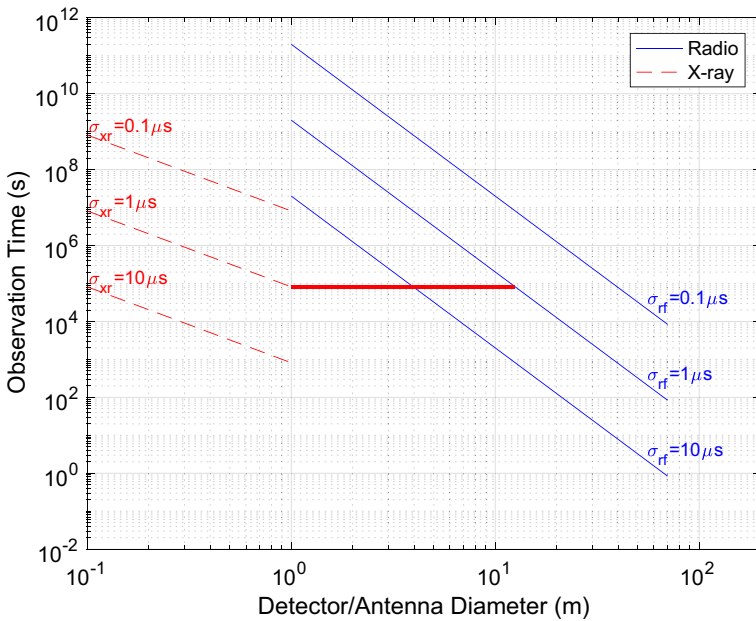

Fig. 6 Required observation time for a given timing accuracy and detector size for B1937+21

From Eq. 15, V_{rf} is a function of the system temperature, T_{sys}, and the receiver bandwidth Δf. It is independent of the antenna size, A; therefore, from Eq. 27 $\sigma_{rf}^2 \propto 1/A^2 \propto 1/d^4$, whereas from Eq. 28 $\sigma_{xr}^2 \propto 1/A \propto 1/d^2$. This difference implies that if the antenna size is not a key design consideration, then a radio-based system is more effective at achieving high timing accuracy assuming the other parameters are fixed.

Solving Eq. 27 for T_{obs} gives an expression for the required observation time in terms of antenna size, pulsar parameters and timing accuracy. Performing the same operation on Eq. 28 gives an analogous expression for the radio-based system. Figures 5, 6 and 7 plot the two resulting expressions for three different millisecond pulsars. These plots compare the impact of the measurement noise on timing accuracy. Table 1 shows the pulsar and the system parameters used in the comparison. The pulsar profiles and parameters can be obtained from online databases [16, 20]. As a reference, the T_{sys} of the RadioAstron space-based radio telescope is 45 K at L-band [17]. In this study, we chose 50 K for the analysis to be conservative. For the X-ray based approach, we used the system parameters of the NICER detector as the baseline [34].

Due to the variations in the pulsar parameters and profiles, the vertical position of the curves in the plots can change drastically from one pulsar to another. From the plots, a 1 m diameter X-ray detector has a similar performance as a 4 m, 12 m and 27 m diameter antenna for J0437-4715, B1937+21 and J2124-3358 respectively at 1-sigma of 1 μs. Since the minimum number of pulsars needed for navigation in the
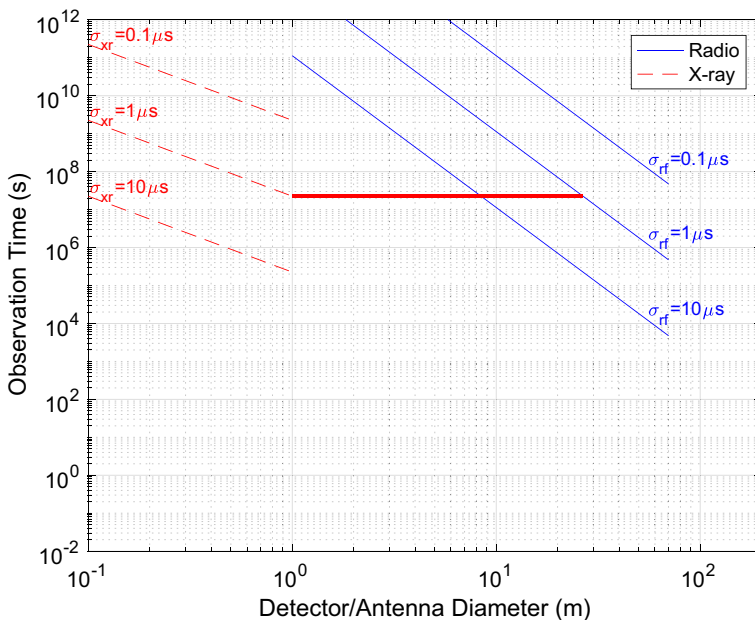

Fig. 7 Required observation time for a given timing accuracy and detector size for J2124-3358

Table 1 Parameters for the Comparison [16, 17, 20, 34]

Pulsar Name	Units	J0347-4715	B1937+21	J2124-3358
$\dot{\phi}$	Hz	174	641	203
$\tilde{\lambda}_{s,xr}$	$ph/(s\ cm^2)$	1.57×10^{-4}	1.61×10^{-5}	4.11×10^{-5}
$\tilde{\lambda}_{b,xr}$	$ph/(s\ cm^2)$	3.44×10^{-4}	1.33×10^{-4}	1.11×10^{-4}
η_{xr}			0.281	
$\tilde{\lambda}_{s,rf}$	mJy	149	13.2	3.6
T_{sys}	K		50	
Δf	MHz		32	
η_{rf}			0.5	
n_p			1	

absence of clock error is 3, one would expect a relatively large radio antenna is still needed to achieve accuracy comparable to the X-ray based system.

Navigation Accuracy for Periodic Thrusting Schedule

Continuing the development from the previous section, this section considers the covariance analysis for the 3-dimensional navigation problem. From the ephemeris of Dawn, it is clear that the use of an ion thruster is associated with a periodic thrusting schedule. In this case, the typical thrusting segment lasts several days and is followed by a few hours of coasting. Similar to the Dawn simulation in the previous section, it was assumed that the spacecraft is only allowed to observe pulsars sequentially during coasting segments. However, instead of using Eq. 4 as the system dynamics, a double integrator system is used to simplify the analysis. Let the state space system be

$$
\begin{bmatrix} \dot{\boldsymbol{r}}_{sc}(t) \\ \ddot{\boldsymbol{r}}_{sc}(t) \end{bmatrix} = \underbrace{\begin{bmatrix} 0 & I_{3x3} \\ 0 & 0 \end{bmatrix}}_{F} \underbrace{\begin{bmatrix} \boldsymbol{r}_{sc}(t) \\ \dot{\boldsymbol{r}}_{sc}(t) \end{bmatrix}}_{\boldsymbol{x}(t)} + \underbrace{\begin{bmatrix} 0 \\ I_{3x3} \end{bmatrix}}_{G} \boldsymbol{w}(t) + \begin{bmatrix} 0 \\ I_{3x3} \end{bmatrix} \boldsymbol{u}(t)
$$
$$
y_p(t) = h_p(t, \boldsymbol{r}_{sc}(t)) + v_p(t), \tag{30}
$$

where $\boldsymbol{r}_{sc}(t)$ is spacecraft position vector; $\dot{\boldsymbol{r}}_{sc}(t)$ is the velocity vector; $\boldsymbol{w}(t)$ is the ion thruster process noise; $\boldsymbol{u}(t)$ is the ion thruster input; and $v_p(t)$ is measurement noise. The measurement function is

$$
h_p(t, \boldsymbol{r}_{sc}) = \lambda_{b,p} + \lambda_{s,p} s_p(\phi_{sc,p}(t))
$$
$$
\phi_{sc,p}(t) = \phi_{0,p} + \dot{\phi}_p \left[t + \frac{\boldsymbol{n}_p^T \boldsymbol{r}_{sc}(t)}{c} - t_{0,p} \right], \tag{31}
$$

where $\lambda_{b,p}$ is background signal intensity; $\lambda_{s,p}$ is pulsar signal intensity; $s_p(\cdot)$ is a periodic function; $\boldsymbol{n}_p$ is the pulsar direction; $\dot{\phi}_p$ is the pulsar frequency; and p is the pulsar index.

The process noise PSD, $W(t)$, and the thrust $\boldsymbol{u}(t)$ are assumed to be constant during the thrusting segment. During the coasting segment, $\boldsymbol{u}(t) = 0$ and $W(t) = 0$. Assuming an EKF is used to process pulsar waveform measurements, then the error covariance is governed by the Riccati equation, here and below

$$\dot{P}(t) = FP(t) + P(t)F^T + GW(t)G^T - P(t)H^T(t)V^{-1}(t)H(t)P(t)$$
$$P(t_0) = P_0, \tag{32}$$

where

$$H(t) = \begin{bmatrix} h'_1(\phi_{sc,p}(t)) & & 0 \\ & \ddots & \\ 0 & & h'_p(\phi_{sc,p}(t)) \end{bmatrix} \begin{bmatrix} \left[\dot{\phi}_1 \frac{\boldsymbol{n}_1^T}{c} \ 0 \right] \\ \vdots \\ \left[\dot{\phi}_p \frac{\boldsymbol{n}_p^T}{c} \ 0 \right] \end{bmatrix}$$
$$V(t) = \mathrm{diag}([V_1(t), \ldots, V_p(t)]), \quad p = 1, \ldots, N_p. \tag{33}$$

The phase, $\phi_{sc,p}(t)$, is evaluated along the true trajectory.

Since there are no pulsar observations during thrusting segments and no thrusting occurs while making pulsar observations, the differential Riccati equation in Eq. 32 reduces to two Lyapunov differential equations. Let the time axis be partitioned as follows:

1. If t is between t_k and t_{k+1}, where k is odd, then this segment is defined as a thrusting segment.
2. If t is between t_k and t_{k+1}, where k is even, then this segment is defined as a coasting segment.

Using the above partition, the Lyapunov differential equation for the thrusting segment is

$$\dot{M}(t) = FM(t) + M(t)F^T + GW(t_k)G^T, \tag{34}$$

where the initial condition is $M(t_k) = P(t_k)$. The solution for Eq. 34 is

$$M(t_{k+1}) = e^{F(t_{k+1}-t_k)} M(t_k) e^{F^T(t_{k+1}-t_k)}$$
$$+ \int_{t_k}^{t_{k+1}} e^{F(t_{k+1}-t)} GW(t_k)G^T e^{F^T(t_{k+1}-t)} dt$$
$$= \Phi_{thr}(\Delta t_k^{thr}) M(t_k) \Phi_{thr}^T(\Delta t_k^{thr}) + \begin{bmatrix} \frac{W(t_k)}{3} \Delta t_k^{thr\,3} & \frac{W(t_k)}{2} \Delta t_k^{thr\,2} \\ \frac{W(t_k)}{2} \Delta t_k^{thr\,2} & W(t_k) \Delta t_k^{thr} \end{bmatrix}, \tag{35}$$

where

$$\Phi_{thr}(\Delta t_k^{thr}) = \begin{bmatrix} I_{3x3} & \Delta t_k^{thr} I_{3x3} \\ 0 & I_{3x3} \end{bmatrix} \tag{36}$$

and $W(t_k)$ is the noise PSD for the kth segment. The error covariance at the end of the thrusting segment is $P(t_{k+1}) = M(t_{k+1})$. The thrusting duration is $\Delta t_k^{thr} = t_{k+1} - t_k$, where k is odd. Because of the process noise, the increase in position error bound is proportional to $\sqrt{\Delta t^3}$ while the velocity error bound is proportional to $\sqrt{\Delta t}$.

The Lyapunov differential equation for the coasting segment is

$$\dot{X}(t) = -F^T X(t) - X(t)F + H^T(t)V^{-1}(t)H(t), \tag{37}$$

where the initial condition is $X(t_k) = P^{-1}(t_k)$. Since we assumed there is no process noise, $w(t)$, or thruster input, $u(t)$, during the coasting segment, the spacecraft trajectory during this segment has constant velocity, i.e., $r_{sc}(t) = r_{sc}(t_k) + \dot{r}_{sc}(t_k)(t - t_k)$. Therefore, the phase equation is

$$\phi_{sc,p}(t) = f_{s,p}(t_k)t + \psi_p(t_k), \tag{38}$$

where

$$f_{s,p}(t_k) = \dot{\phi}_p \left[1 + \frac{n_p^T \dot{r}_{sc}(t_k)}{c} \right]$$

$$\psi_p(t_k) = \phi_{0,p} + \dot{\phi}_p \left[\frac{n_p^T [r_{sc}(t_k) - \dot{r}_{sc}(t_k)t_k]}{c} - t_{0,p} \right]. \tag{39}$$

The form of Eq. 38 implies that the pulsar signals have constant frequencies and constant phase offsets during coasting segments. Since we only consider sequential observation, the coasting duration can be partitioned into multiple sub-segments,

$$\Delta t_k^{coast} = t_{k+1} - t_k = \sum_{p=1}^{N_p} \Delta t_{k,p}^{obs}, \tag{40}$$

where k is even. This simplification implies the dimension of the measurement matrix over each sub-segment is reduced to 1×6. This reduced matrix is denoted as $H_p(t)$, which is the pth row of $H(t)$. The pulsar observation duration is $\Delta t_{k,p}^{obs} = t_{k,p}^e - t_{k,p}^s$, where $t_{k,p}^s$ and $t_{k,p}^e$ are the observation starting and ending times of the pth pulsar in the kth time segment. Let $t_k = t_{k,1}^s$, $t_{k,p}^e = t_{k,p+1}^s$, and $t_{k+1} = t_{k,N_p}^e = t_{k,N_p+1}^s$, then the solution for Eq. 37 can be written as

$$X(t_{k,p}^e) = e^{-F^T(t_{k,p}^e - t_{k,p}^s)} X(t_{k,p}^s) e^{-F(t_{k,p}^e - t_{k,p}^s)}$$

$$+ \int_{t_{k,p}^s}^{t_{k,p}^e} e^{-F^T(t_{k,p}^e - t)} H_p^T(t) V_p^{-1}(t) H_p(t) e^{-F(t_{k,p}^e - t)} dt$$

$$= \tilde{\Phi}_{obs}(\Delta t_{k,p}^{obs}) X(t_{k,p}^s) \tilde{\Phi}_{obs}^T(\Delta t_{k,p}^{obs}) + Q_p(\Delta t_{k,p}^{obs}), \tag{41}$$

where

$$
\begin{aligned}
Q_p(\Delta t_{k,p}^{obs}) &= \int_{t_{k,p}^s}^{t_{k,p}^e} \begin{bmatrix} I & 0 \\ -(t_{k,p}^e - t)I & I \end{bmatrix} \begin{bmatrix} \dot{\phi}_p \frac{n}{c} \\ 0 \end{bmatrix} \frac{h_p'^2(\phi_{sc,p}(t))}{V_p(t)} \begin{bmatrix} \dot{\phi}_p \frac{n^T}{c} & 0 \end{bmatrix} \begin{bmatrix} I & -(t_{k,p}^e - t)I \\ 0 & I \end{bmatrix} dt \\
&= \frac{\dot{\phi}_p^2}{c^2} \int_{t_{k,p}^s}^{t_{k,p}^e} \frac{h_p'^2(\phi_{sc,p}(t))}{V_p(t)} \begin{bmatrix} \Xi_p & -(t_{k,p}^e - t)\Xi_p \\ -(t_{k,p}^e - t)\Xi_p & (t_{k,p}^e - t)^2 \Xi_p \end{bmatrix} dt \\
&= \frac{\dot{\phi}_p^2}{c^2} \int_0^{\Delta t_{k,p}^{obs}} \frac{h_p'^2(\phi_{sc,p}(t_{k,p}^s + \tau))}{V_p(t_{k,p}^s + \tau)} \begin{bmatrix} \Xi_p & -\left(\Delta t_{k,p}^{obs} - \tau\right)\Xi_p \\ -\left(\Delta t_{k,p}^{obs} - \tau\right)\Xi_p & \left(\Delta t_{k,p}^{obs} - \tau\right)^2 \Xi_p \end{bmatrix} d\tau \\
\Xi_p &= n_p n_p^T,
\end{aligned}
\tag{42}
$$

and

$$
\tilde{\Phi}_{obs}(\Delta t_{k,p}^{obs}) = \begin{bmatrix} I_{3x3} & 0 \\ -\Delta t_{k,p}^{obs} I_{3x3} & I_{3x3} \end{bmatrix}.
\tag{43}
$$

for $p = 1, \ldots, N_p$. Note the change in integration variable, $\tau = t - t_{k,p}^s$, in Eq. 42. The symbol $f'(x)$ indicates the derivative of $f(x)$ with respect to x.

If radio pulsars are used, then $V_p(t)$ is a constant representing the Gaussian radiometer noise PSD. If X-ray pulsars are used, then $V_p(t) = \lambda_{b,p} + \lambda_{s,p} s_p(\phi_{sc,p}(t))$ for a non-homogenous Poisson process. If the observation time is much larger than the signal period ($\Delta t_{k,p}^{obs} \gg 1/f_{s,k,p}$), then the integrals in Eq. 42 can be approximated using the following expressions [10],

$$
\int_0^{\Delta t_{k,p}^{obs}} \frac{h_p'^2(\phi_{sc,p}(T + \tau))}{V_p(T + \tau)} d\tau \approx \Delta t_{k,p}^{obs} I_p
$$

$$
\int_0^{\Delta t_{k,p}^{obs}} \frac{\tau h_p'^2(\phi_{sc,p}(T + \tau))}{V_p(T + \tau)} d\tau \approx \frac{\Delta t_{k,p}^{obs 2}}{2} I_p
$$

$$
\int_0^{\Delta t_{k,p}^{obs}} \frac{\tau^2 h_p'^2(\phi_{sc,p}(T + \tau))}{V_p(T + \tau)} d\tau \approx \frac{\Delta t_{k,p}^{obs 3}}{3} I_p,
\tag{44}
$$

where

$$
I_p = \int_0^1 \frac{\lambda_{s,p}^2 s_p'^2(\theta)}{V_p(\theta)} d\theta,
\tag{45}
$$

and T is a constant time offset. The above approximation is only valid for signals with constant frequencies, and it removes the dependence on spacecraft position and

velocity for linearization. In other words, for this simplified model, the navigation accuracy is insensitive to the spacecraft states. Substituting Eq. 44 into Eq. 42 gives

$$
\begin{aligned}
X(t_{k,p}^e) &\approx \tilde{\Phi}_{obs}(\Delta t_{k,p}^s) X(t_{k,p}^s) \tilde{\Phi}_{obs}^T(\Delta t_{k,p}^s) \\
&+ \frac{\dot{\phi}_p^2 I_p}{c^2}
\begin{bmatrix}
\Delta t_{k,p}^{obs} \, \Xi_p & -\left(\Delta t_{k,p}^{obs\,2} - \frac{\Delta t_{k,p}^{obs\,2}}{2}\right)\Xi_p \\
-\left(\Delta t_{k,p}^{obs\,2} - \frac{\Delta t_{k,p}^{obs\,2}}{2}\right)\Xi_p & \left(\Delta t_{k,p}^{obs\,3} - 2\frac{\Delta t_{k,p}^{obs\,3}}{2} + \frac{\Delta t_{k,p}^{obs\,3}}{3}\right)\Xi_p
\end{bmatrix} \\
&\approx \tilde{\Phi}_{obs}(\Delta t_{k,p}^s) X(t_{k,p}^s) \tilde{\Phi}_{obs}^T(\Delta t_{k,p}^s) + \frac{\dot{\phi}_p^2 I_p}{c^2}
\begin{bmatrix}
\Delta t_{k,p}^{obs} \, \Xi_p & -\frac{\Delta t_{k,p}^{obs\,2}}{2}\Xi_p \\
-\frac{\Delta t_{k,p}^{obs\,2}}{2}\Xi_p & \frac{\Delta t_{k,p}^{obs\,3}}{3}\Xi_p
\end{bmatrix}. \quad (46)
\end{aligned}
$$

Equation 46 is the information matrix at the end of a pulsar observation, $t_{k,p}^e$. In order to discuss the positioning accuracy, Eq. 46 has to be inverted to obtain the error covariance, $P(t_{k,p}^e)$.

Given the system in Eq. 30, the state transition matrix for one pulsar observation is

$$
\begin{aligned}
\Phi_{obs}(\Delta t_{k,p}^{obs}) &= \begin{bmatrix} I_{3x3} & \Delta t_{k,p}^{obs} I_{3x3} \\ 0 & I_{3x3} \end{bmatrix} \\
&= \tilde{\Phi}_{obs}^{-T}(\Delta t_{k,p}^{obs}). \quad (47)
\end{aligned}
$$

Therefore, the error covariance not including the measurement update at the end of the observation is

$$
\begin{aligned}
M(t_{k,p}^e) &= \Phi_{obs}(\Delta t_{k,p}^{obs}) P(t_{k,p}^s) \Phi_{obs}^T(\Delta t_{k,p}^{obs}) \\
&= \tilde{\Phi}_{obs}^{-T}(\Delta t_{k,p}^{obs}) P(t_{k,p}^s) \tilde{\Phi}_{obs}^{-1}(\Delta t_{k,p}^{obs}) \\
&= \left(\tilde{\Phi}_{obs}(\Delta t_{k,p}^{obs}) X(t_{k,p}^s) \tilde{\Phi}_{obs}^T(\Delta t_{k,p}^{obs})\right)^{-1}. \quad (48)
\end{aligned}
$$

Factoring Eq. 46 gives

$$
X(t_{k,p}^e) \approx \underbrace{\tilde{\Phi}_{obs}(\Delta t_{k,p}^{obs}) X(t_{k,p}^s) \tilde{\Phi}_{obs}^T(\Delta t_{k,p}^{obs})}_{M^{-1}(t_{k,p}^e)}
$$

$$
+ \underbrace{\begin{bmatrix} \dot{\phi}_p \frac{\boldsymbol{n}_p}{c} & 0 \\ 0 & \dot{\phi}_p \frac{\boldsymbol{n}_p}{c} \end{bmatrix}}_{\tilde{H}_p^T} I_p \underbrace{\begin{bmatrix} \Delta t_{k,p}^{obs} & -\frac{\Delta t_{k,p}^{obs\,2}}{2} \\ -\frac{\Delta t_{k,p}^{obs\,2}}{2} & \frac{\Delta t_{k,p}^{obs\,3}}{3} \end{bmatrix}}_{\tilde{V}_p^{-1}(\Delta t_{k,p}^{obs})} \underbrace{\begin{bmatrix} \dot{\phi}_p \frac{\boldsymbol{n}_p}{c} & 0 \\ 0 & \dot{\phi}_p \frac{\boldsymbol{n}_p}{c} \end{bmatrix}^T}_{\tilde{H}_p}. \quad (49)
$$

Applying the matrix inversion lemma gives

$$
\begin{aligned}
P(t_{k,p}^e) &\approx M(t_{k,p}^e) - M(t_{k,p}^e) \tilde{H}_p^T \left(\tilde{H}_p M(t_{k,p}^e) \tilde{H}_p^T + \tilde{V}_p(\Delta t_{k,p}^{obs})\right)^{-1} \tilde{H}_p M(t_{k,p}^e) \\
&\approx \left(I - \tilde{K}_p(t_{k,p}^e)\tilde{H}_p\right) M(t_{k,p}^e) \left(I - \tilde{K}_p(t_{k,p}^e)\tilde{H}_p\right)^T \\
&\quad + \tilde{K}_p(t_{k,p}^e) \tilde{V}_p(\Delta t_{k,p}^{obs}) \tilde{K}_p^T(t_{k,p}^e), \quad (50)
\end{aligned}
$$

where

$$\tilde{K}_p(t_{k,p}^e) = M(t_{k,p}^e)\tilde{H}_p^T \left(\tilde{H}_p M(t_{k,p}^e)\tilde{H}_p^T + \tilde{V}_p(\Delta t_{k,p}^{obs})\right)^{-1},$$

$$\tilde{V}_p(\Delta t_{k,p}^{obs}) = \frac{2}{I_p}\begin{bmatrix} \frac{2}{\Delta t_{k,p}^{obs}} & \frac{3}{\Delta t_{k,p}^{obs\,2}} \\ \frac{3}{\Delta t_{k,p}^{obs\,2}} & \frac{6}{\Delta t_{k,p}^{obs\,3}} \end{bmatrix}. \tag{51}$$

The error covariance at the start of the next observation is equal to that at the end of the previous observation, $P(t_{k,p+1}^s) = P(t_{k,p}^e)$. The error covariance at the end of each coasting segment is $P(t_{k+1}) = P(t_{k,N_p+1}^s)$. The matrices $\tilde{H}_p$, $\tilde{K}_p$, and $\tilde{V}_p$ can be interpreted as the effective measurement matrix, the effective filter gain, and the effective noise covariance matrix. They show the measured pulsar signal over the observation time, $\Delta t_{k,p}^{obs}$, not only provides position information but also velocity information. From the form of Eq. 50, the navigation pulsars should have high signal frequency and large I_p. From Eq. 45, I_p is large when the signal-to-noise ratio is high. The impact of the pulsar waveform profile is also accounted for by the integral. Longer observation duration also improves the navigation accuracy. The impact of the pulsar geometry on the covariance matrix is more difficult to recognize, so it is necessary to evaluate Eq. 50 numerically.
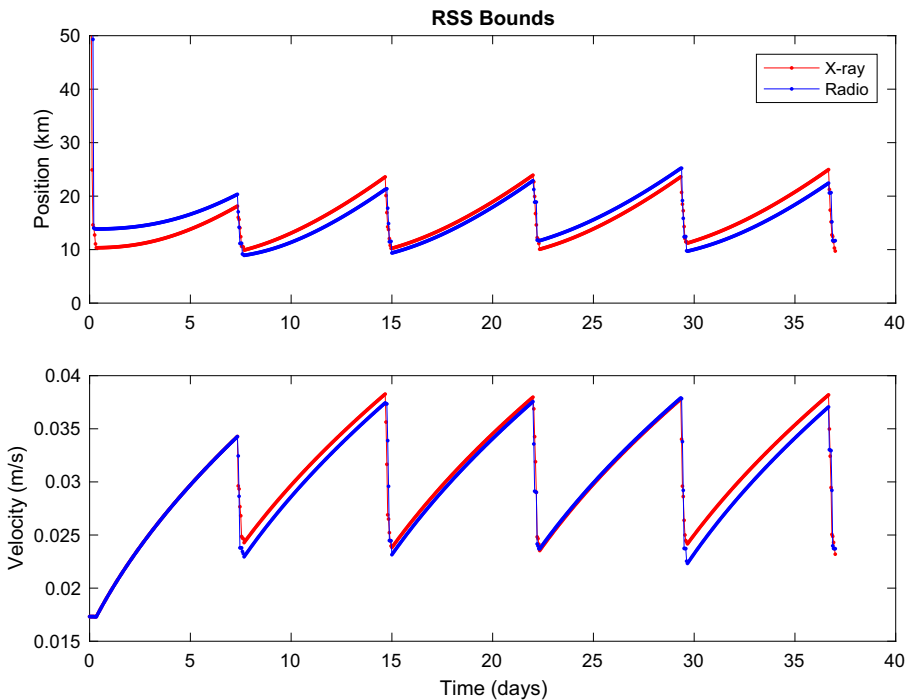

Fig. 8 Covariance analysis for periodic thrusting schedule

Table 2 Radio Pulsar Parameters [20]

Obsv. order	Pulsar name	$\lambda_{b,rf}$ (K)	$\lambda_{s,rf}$ (mK)	$\tilde{\lambda}_{s,rf}$ (mJy)	$\dot{\phi}$ (Hz)	RA $(°)$	DEC $(°)$
1	J0437-4715	50	2.564	149.0	173.7	69.32	−47.25
2	J0711-6830	50	0.055	3.2	182.1	107.98	−68.51
3	J1045-4509	50	0.046	2.7	133.8	161.46	−45.17
4	J1713+0747	50	0.176	10.2	218.8	258.46	7.79
5	B1937+21	50	0.227	13.2	641.9	294.91	21.58

RA is right ascension and DEC is declination in the celestial coordinate system

Equation 34 and 50 can be evaluated in an alternating manner to compute the error covariance of the EKF for the system in Eq. 30. The thrusting and observation schedule used in generating Fig. 8 consists of 5 thrusting segments and 4 coasting segments. Each thrusting segment is 7 days and each coasting segment is 8 hours. In other words, the thrusting duty cycle is 95%. Gates parameters for the process noise are $\sigma_{fixed,i} = 10^{-10}$ km/s^2 and $\sigma_{prop,i} = 0.44\%$ for $i = 1, 2, 3$. The acceleration magnitude over each thrusting segment is constant at 8×10^{-5} m/s^2. Both the radio-based and the X-ray based systems observe the first 5 pulsars listed in Table 2 and Table 3 sequentially. The observation duration for each pulsar is 1 hour for both cases. The radiometer noise PSD is calculated by substituting $\eta_{rf} = 0.5$, $n_p = 1$, $\Delta f = 32$ MHz, and $T_{sys} = 50$ K into Eq. 15, where the antenna diameter is set to 11 m. The initial XYZ position and XYZ velocity 1-sigma bounds are 50 km and 0.01 m/s respectively.

Because of the addition of the process noise during each thrusting segment, the position error bound exhibits a periodic-like pattern. Therefore, it is necessary to allocate sufficient observation time to keep the position error bound to within ±0.5 cyc of the wavelength of the fastest pulsar. In this analysis, the radio antenna is sized such that the radio-based system has a similar performance to the X-ray based system. Once the system is in a periodic-like steady state, the Root-Sum-Square (RSS) position bounds for both systems at the start of the coasting segment are approximately

Table 3 X-ray Pulsar Parameters [20, 34]

Obsv. order	Pulsar name	$\lambda_{b,xr}$ (ph/s)	$\lambda_{s,xr}$ (ph/s)	$\dot{\phi}$ (Hz)	RA $(°)$	DEC $(°)$
1	J0437-4715	0.62	0.283	173.7	69.32	−47.25
2	J0030+0451	0.20	0.193	205.5	7.61	4.86
3	J2124-3358	0.20	0.074	202.8	321.18	−33.98
4	J0218+4232	0.20	0.082	430.5	34.53	42.54
5	B1821-24	0.22	0.093	327.9	270.4	−24.87
6	B1937+21	0.24	0.029	641.9	294.9	21.6

RA is right ascension and DEC is declination in the celestial coordinate system

25 km. At the end of the coasting segment they reduce to approximately 12 km. This pattern repeats for every thrusting and coasting pair.

Particle Filter for Position Acquisition

In the integer ambiguity problem with sequential pulsar measurements, we used a basic particle filter with resampling and roughening [1, 31]. Traditional methods such as hypothesis testing and floating-point integer estimation are not directly applicable to pulsar-based navigation because of the following reasons [36, 37]. Due to design considerations on size, weight, and power, it is unlikely that a deep space exploration spacecraft would carry multiple X-ray detectors for navigation purposes. Furthermore, since X-ray pulsar signals have low signal-to-noise ratio compared to the GPS for example, extended observation time on the order of tens of minutes is required to obtain the fractional part of the differential phase measurement and the Doppler frequency measurement. Coupling these difficulties with large uncertainty in spacecraft velocity makes it impractical to track multiple pulsar signals simultaneously and continuously. Having large velocity uncertainty means the pulsar phase measurement between two observations cannot be connected using state prediction. Therefore, the position acquisition method has to be able to resolve the integer associated with each pulsar sequentially relying only on the fractional phase. The idea of using a particle filter to resolve the integer ambiguity in differential GPS phase measurement has been investigated in prior research [14]. This section extends that idea to pulsar-based navigation.

The particle filter relies on the sequential Monte Carlo method, in which a large number of particles are generated to approximate the conditional Probability Density Function (PDF),

$$p(\boldsymbol{x}_k|z_k) \approx \sum_{i=1}^{N} w_k^i \delta(\boldsymbol{x}_k - \boldsymbol{x}_k^i), \tag{52}$$

where $\boldsymbol{x}_k^i$ and w_k^i are the particle and the associated weight at time t_k respectively. The number of particles is denoted by N. The state can be estimated by taking the sum of each particle's state, weighted by the conditional PDF of that particle. The unnormalized weight of the ith particle at time t_k is

$$\check{w}_k^i = \frac{p(z_k|\boldsymbol{x}_k^i)p(\boldsymbol{x}_k^i|\boldsymbol{x}_{k-1}^i)w_{k-1}^i}{q(\boldsymbol{x}_k^i|\boldsymbol{x}_{k-1}^i, z_k)}$$

$$w_k^i = \frac{\check{w}_k^i}{\sum_{i=1}^{N} \check{w}_k^i}. \tag{53}$$

$p(z_k|\boldsymbol{x}_k)$ is the likelihood function; $p(\boldsymbol{x}_k|\boldsymbol{x}_{k-1})$ is the transition density function; w_{k-1} is the normalized weight from the previous time step; and $q(\boldsymbol{x}_k|\boldsymbol{x}_{k-1}, z_k)$ is the proposal density function for drawing the particles. Setting the proposal density

function, $q(\boldsymbol{x}_k|\boldsymbol{x}_{k-1}, z_k)$, to the transition density function, $p(\boldsymbol{x}_k|\boldsymbol{x}_{k-1})$, simplifies Eq. 53 to

$$\check{w}_k^i = p(z_k|\boldsymbol{x}_k^i)w_{k-1}^i. \tag{54}$$

This choice means that $\boldsymbol{x}_k^i \sim p(\boldsymbol{x}_k|\boldsymbol{x}_{k-1}^i)$. Because Eq. 54 is the same as the sequential Wald probability ratio test used in the GPS integer ambiguity resolution problem, one can view the measurement update step of the particle filter as hypothesis testing [37].

Since the particle filter is used for position acquisition, a simplified dynamical model is used instead of Eq. 23.

$$\ddot{\boldsymbol{r}}_{sc}(t) = -\frac{\mathcal{G}m_\odot}{\|\boldsymbol{r}_{sc}(t)\|^3}\boldsymbol{r}_{sc}(t) + \boldsymbol{w}_r(t). \tag{55}$$

Furthermore, we assumed the fractional part of the differential phase measurement and the Doppler frequency measurement are available from a MLE [10]. Under these assumptions the measurement equation for the particle filter is

$$\boldsymbol{z}_p(t) = \begin{bmatrix} \dot{\phi}_p \dfrac{\boldsymbol{n}_p^T \boldsymbol{r}_{sc}(t)}{c} - N_p(t) \\ \dot{\phi}_p \dfrac{\boldsymbol{n}_p^T \dot{\boldsymbol{r}}_{sc}(t)}{c} \end{bmatrix} + \boldsymbol{v}_p(t), \tag{56}$$

where the number of integer wavelengths from the SSB to the spacecraft is

$$N_p(t) = \begin{bmatrix} \dot{\phi}_p \dfrac{\boldsymbol{n}_p^T \boldsymbol{r}_{sc}(t)}{c} \end{bmatrix}_{int}, \tag{57}$$

and p is the pulsar index. The function $[\cdot]_{int}$ rounds the argument to the nearest integer, which means the true fractional phase is between -0.5 and 0.5. The measurement noise, $\boldsymbol{v}_p(t)$, is assumed to be Gaussian and white. The covariance is set according to the CRLB associated with the pulsar phase and frequency estimation problem,

$$\sigma_{CRLB,p}^2 = \frac{2}{I_p} \begin{bmatrix} \dfrac{2}{T_{obs}} & \dfrac{-3}{T_{obs}^2} \\ \dfrac{-3}{T_{obs}^2} & \dfrac{6}{T_{obs}^3} \end{bmatrix}, \tag{58}$$

where T_{obs} is the observation time and I_p is given by Eq. 45.

The high-level particle filter algorithm is as follows:

1. Propagate N particles according to Eq. 55 with different process noise realizations from t_{k-1} to t_k.
2. Observe a pulsar to obtain fractional phase and Doppler frequency measurements subject to measurement noise (Eq. 56).
3. Evaluate the likelihood function of each particle based on which a normalized weight is assigned (Eq. 54).
4. Compute the best estimate and empirical covariance from the weighted sum of these particles.
5. If the effective number of particles, N_{eff}, is below a specified threshold, N_{thr}, resample and roughen the particles.

Sample degeneracy occurs when only a few particles have high weights. This occurs in cases where the initial sample space is large so that only a relatively small

number of particles will be close to the true state. The high weight particles will tend to increase in weight until only a single particle represents the entire conditional PDF. This will cause divergence of the filter and the empirical covariance to approach zero. Sample degeneracy may be countered by resampling, but naive resampling can lead to "sample impoverishment." For instance, if one simply replaces low weight particles with copies of high weight particles, all the particles and thus weights will be identical. Both these problems arise because we are attempting to estimate the conditional PDF, a continuous function, with discrete particles. Ideally, we could resample the particles from the continuous conditional PDF. However, because the conditional PDF is only known at discrete values calculated from the particles, the only guaranteed way to approach the continuous conditional PDF distribution is to increase the particle count. If the initial uncertainty is large, this can lead to an intractably large number of particles. This is because the number of particles needed is proportional to the volume of the phase space, which is 6-dimensional.

In step 5, the particles are resampled using the systematic resampling method [1]. The criterion for resampling is given by the effective number of particles,

$$N_{eff} = \frac{1}{\sum_{i=1}^{N}(w_k^i)^2} \tag{59}$$

where N_{eff} ranges from 1 to N. It is 1 if all the particles are weight 0 except for one, and N if all the particles are weight $1/N$. Thus, it is a useful statistic for determining the variance of the particles and how many of them are close to the true state. The threshold for resampling was chosen to be $N_{thr} = N/2$.

To alleviate the sample impoverishment issue, the roughening step adds three noises to the resampled particles,

$$x_k^i = \tilde{x}_k^i + \epsilon_{1,k} + \epsilon_{2,k} + \epsilon_{3,k}, \tag{60}$$

where

$$\epsilon_{1,k} \sim \mathcal{N}(0, \tilde{P}_1(t_k)), \quad \epsilon_{2,k} \sim \mathcal{N}(0, \tilde{P}_2(t_k)), \quad \epsilon_{3,k} \sim \mathcal{N}(0, \tilde{P}_3(t_k)), \tag{61}$$

and $\tilde{x}_k^i$ is from the particle set after resampling. The first noise, $\epsilon_{1,k}$, is drawn from a Gaussian distribution with covariance, $\tilde{P}_1(t_k) = C_1 P(t_k) C_1^T$. Thus, as the filter processes more measurements the first term decays with time. This term is added to increase sample diversity during filter initialization. The second noise, $\epsilon_{2,k}$, is drawn from a Gaussian distribution with covariance, $\tilde{P}_2(t_k) = C_2 P(t_0) C_2^T$. This noise term is always present and ensures particle diversity during steady state. The two tuning matrices have the form

$$C_1 = \begin{bmatrix} c_{11} I_{3x3} & 0 \\ 0 & c_{12} I_{3x3} \end{bmatrix}, \quad C_2 = \begin{bmatrix} c_{21} I_{3x3} & 0 \\ 0 & c_{22} I_{3x3} \end{bmatrix}. \tag{62}$$

The third noise, $\epsilon_{3,k}$, is also drawn from a Gaussian distribution; however, this term places particles in the direction with high measurement likelihood to enable the filter to more efficiently search for the spacecraft position. This term is included

to address the limited number of particles and large initial position uncertainty. The covariance for $\epsilon_{3,k}$ is

$$\tilde{P}_3(t_k) = \begin{bmatrix} L_k S_k L_k^T & 0 \\ 0 & 0 \end{bmatrix} e^{-(k-1)}. \tag{63}$$

The exponential decay term in Eq. 63 ensures $\epsilon_{3,k}$ disappears during steady state. The L_k matrix is a transformation between the inertial frame and a frame specified by two angles: $\tilde{\alpha}$ and $\tilde{\beta}$.

$$L_k = \begin{bmatrix} \cos(\tilde{\alpha}) & -\sin(\tilde{\alpha}) & 0 \\ \sin(\tilde{\alpha}) & \cos(\tilde{\alpha}) & 0 \\ 0 & 0 & 1 \end{bmatrix} \begin{bmatrix} \cos(\tilde{\beta}) & 0 & \sin(\tilde{\beta}) \\ 0 & 1 & 0 \\ -\sin(\tilde{\beta}) & 0 & \cos(\tilde{\beta}) \end{bmatrix} \tag{64}$$

The motivation for $\epsilon_{3,k}$ is based on the following geometric facts. The intersections between a sphere and planes are circular planes; the intersections between planes and planes are lines; and the intersections between planes and lines are points. The sphere represents the initial distribution of the particles at time t_0. Each plane, whose normal vector is $\boldsymbol{n}_p$, represents the region of high measurement likelihood associated with each pulsar measurement. Therefore, after the first measurement update and resampling, the surviving particles tend to lie on several planes. Similarly, after the second and third measurement updates and resampling, the surviving particles tend to lie on several lines and points respectively. One can interpret each point (particle cluster) as a single integer hypothesis. In order to reduce the number of hypotheses and increase the number of particles per hypothesis, it is more advantageous to observe pulsars with longer wavelength during the beginning of the simulation. Observing several different pulsars also increases the speed of convergence because it allows the filter to better distinguish the true hypothesis from the rest.

The roughening direction for $\epsilon_{3,k}$ is given below. In the first resampling step, $k = 1$, the S_k matrix and $\tilde{\alpha}$ and $\tilde{\beta}$ angles are chosen as

$$S_k = \begin{bmatrix} c_3^2 \tilde{\sigma}_p^2 & 0 \\ 0 & c_4^2 I_{2x2} \end{bmatrix}$$

$$\tilde{\alpha} = \text{atan}\,2\left([\boldsymbol{n}_p]_2, [\boldsymbol{n}_p]_1\right)$$

$$\tilde{\beta} = -\text{atan}\,2\left([\boldsymbol{n}_p]_3, \sqrt{[\boldsymbol{n}_p]_1^2 + [\boldsymbol{n}_p]_2^2}\right), \tag{65}$$

where p is the index of the first pulsar. The positioning accuracy of the pth pulsar in the direction of $\boldsymbol{n}_p$ is related to the (1,1) component of the CRLB bound in Eq. 58 and the pulsar frequency,

$$\tilde{\sigma}_p^2 = \frac{c^2}{\phi_p^2}[\sigma_{CRLB,p}^2]_{11}. \tag{66}$$

The tuning parameters c_3 and c_4 in this time step control the magnitude of the out-of-plane and in-plane perturbations. Given the angles in Eq. (65), the matrix, L_k, is a transformation from the inertial frame to a frame whose X-axis is aligned with the pulsar direction, $\boldsymbol{n}_p$.

In the second resampling step, $k = 2$, the S_k matrix and $\tilde{\alpha}$ and $\tilde{\beta}$ angles are chosen as

$$S_k = \begin{bmatrix} c_4^2 & 0 \\ 0 & c_3^2 \tilde{\sigma}_p^2 I_{2x2} \end{bmatrix}$$

$$\tilde{\alpha} = \text{atan } 2\left([\tilde{n}]_2, [\tilde{n}]_1\right)$$

$$\tilde{\beta} = -\text{atan } 2\left([\tilde{n}]_3, \sqrt{[\tilde{n}]_1^2 + [\tilde{n}]_2^2}\right)$$

$$\tilde{n} = n_p \times n_{p-1}. \tag{67}$$

The tuning parameters c_3 and c_4 in this time step control the magnitude of the in-plane and out-of-plane perturbations. Given the angles in Eq. 67, the matrix, L_k, is a transformation from the inertial frame to a frame whose X-axis is aligned with the cross product of the current pulsar direction with the previous pulsar direction. In other words, the out-of-plane direction in this step is along $\tilde{n}$ rather than n_p.

For the third and subsequent steps, $k \geq 3$, the S_k matrix is chosen as

$$S_k = c_3^2 \tilde{\sigma}_p^2 I_{3x3}, \tag{68}$$

and the $\tilde{\alpha}$ and $\tilde{\beta}$ angles are chosen according to Eq. 65. After $k = 3$, the filter uses pulsar measurements to eliminate particle clusters until one only cluster is left. Figure 9 shows the particle distribution due to this roughening strategy at $k = 0, k = 1, k = 2$, and $k = 3$. The bottom right plot shows that every integer ambiguity within a radius of 5200 km around the mean is populated with particles.

Simulation Results

In the following results, an orbiting spacecraft at 1 AU with perpendicular velocity 30 km/s was estimated for $t_f = 5\ day$. Let the initial covariance be partitioned as

$$P(t_0) = \begin{bmatrix} P_{r_{sc}}(t_0) & 0 \\ 0 & P_{\dot{r}_{sc}}(t_0) \end{bmatrix}. \tag{69}$$

The initial velocity covariance is scaled according to the initial position covariance, the mean position vector, and the mean velocity vector,

$$[P_{\dot{r}_{sc}}(t_0)]_{ii} = 10 \times [P_{r_{sc}}(t_0)]_{ii} \left(\frac{\|\dot{\bar{r}}_{sc}(t_0)\|}{\|\bar{r}_{sc}(t_0)\|}\right)^2, \tag{70}$$

for $i = 1...3$. The numerical values of these covariance matrices are $P_{r_{sc}}(t_0) = 9 \times 10^6 I_{3x3}\ km^2$ and $P_{\dot{r}_{sc}}(t_0) = 3.61 I_{3x3}\ m^2/s^2$. In the following realization, the initial XYZ position errors are $[\hat{e}(t_0)]_1 = -3000\ km$, $[\hat{e}(t_0)]_2 = 3000\ km$, and $[\hat{e}(t_0)]_3 = -3000\ km$ respectively. The initial XYZ velocity errors are $[\hat{e}(t_0)]_4 = 2.0\ m/s$, $[\hat{e}(t_0)]_5 = 1.5\ m/s$, and $[\hat{e}(t_0)]_6 = -1.5\ m/s$ respectively. The PSD of the acceleration disturbance is $W_r = 10^{-18}\ I_{3x3}\ km^2/s^3$. It was assumed that the spacecraft carries a body mounted X-ray detector similar to the 56-element NICER X-ray telescope. The spacecraft observes the 6 pulsars listed in Table 3 sequentially with a observation duration of 1 hr for each pulsar. The wavelengths of the pulsars in the table are 1727 km, 1479 km, 1460 km, 697 km, 915 km, and 463 km following
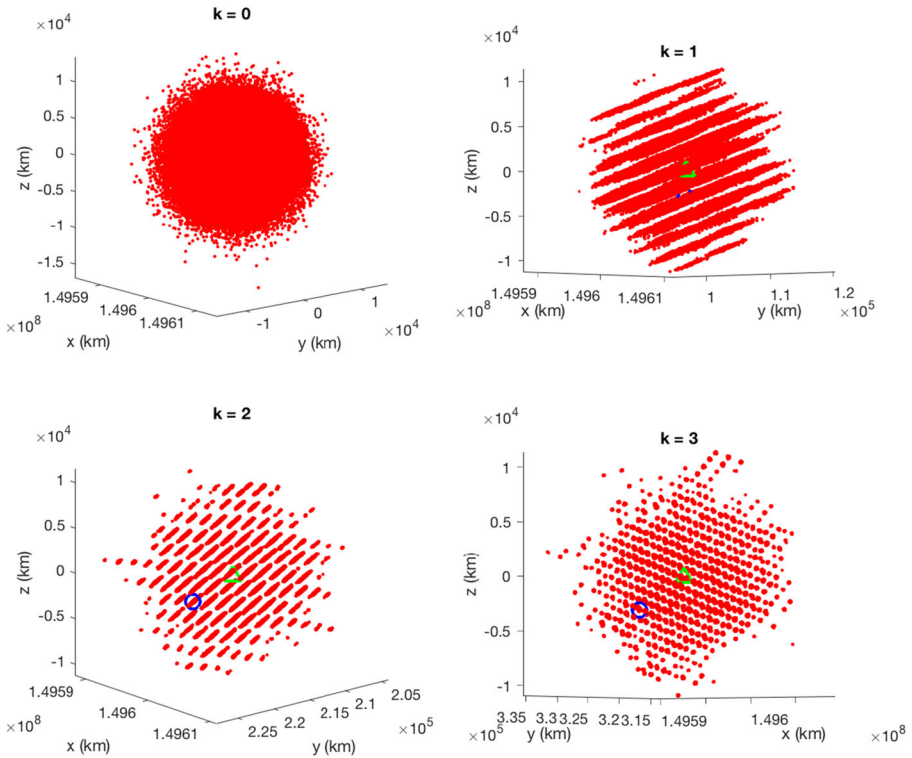
Fig. 9 This figure shows the initial particle distribution and the subsequent 3 time steps. The blue circles are the true spacecraft position and the green triangles are the particle filter position estimates. The particle distribution changes from a sphere at $k = 0$ to several plane segments at $k = 1$ to several line segments at $k = 2$ then to several points at $k = 3$

the listed order. The number of particles was $N = 300000$. The 6 tuning parameters in Eqs. 62, 65, 67 and 68 were

$$c_{11} = c_{12} = 0.01, \quad c_{21} = 0.001, \quad c_{22} = 0.1, \quad c_3 = 0, \quad c_4 = 900. \qquad (71)$$

Let the estimation error and the 1σ error bound be defined as

$$\hat{e}(t_k) = x(t_k) - \hat{x}(t_k)$$
$$\sigma(t_k) = \sqrt{\mathrm{diag}[P(t_k)]}. \qquad (72)$$

The definitions of the RSS errors and bounds are

$$\hat{e}_{rss,r_{sc}}(t_k) = \sqrt{[\hat{e}(t_k)]_1^2 + [\hat{e}(t_k)]_2^2 + [\hat{e}(t_k)]_3^2}$$
$$\hat{e}_{rss,\dot{r}_{sc}}(t_k) = \sqrt{[\hat{e}(t_k)]_4^2 + [\hat{e}(t_k)]_5^2 + [\hat{e}(t_k)]_6^2}$$
$$\sigma_{rss,r_{sc}}(t_k) = \sqrt{[P(t_k)]_{11} + [P(t_k)]_{22} + [P(t_k)]_{33}}$$
$$\sigma_{rss,\dot{r}_{sc}}(t_k) = \sqrt{[P(t_k)]_{44} + [P(t_k)]_{55} + [P(t_k)]_{66}}. \qquad (73)$$
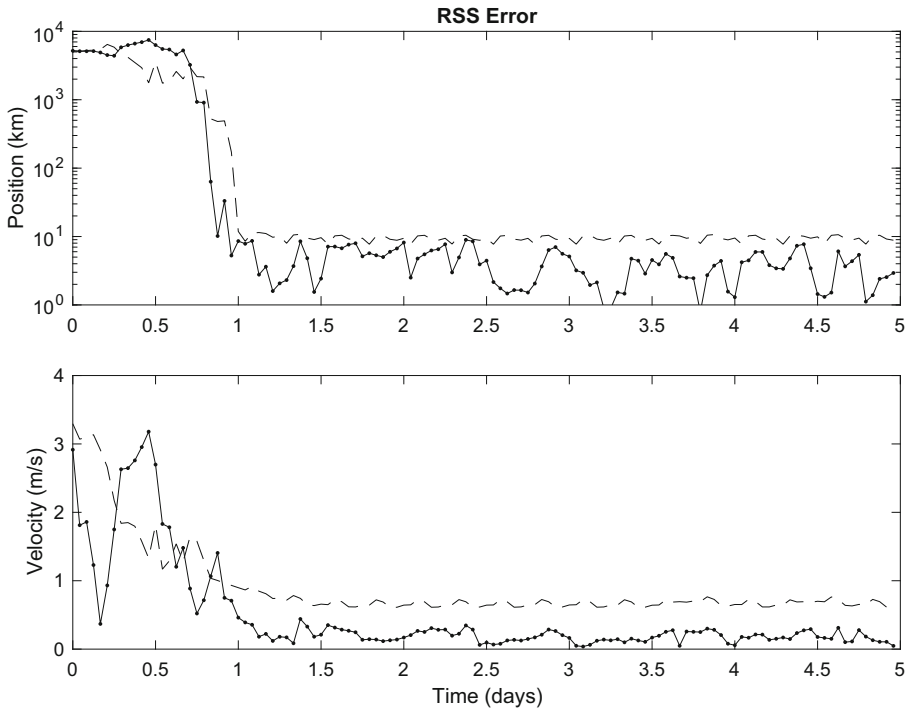
Fig. 10 This figure shows the RSS estimation errors in position and velocity. The black dashed lines are the RSS bounds from the particle filter and the black dots are the estimation errors

The RSS position and velocity errors of a single realization are given in Fig. 10. The convergence of the pulsar integer cycle counts, given by the error in the number of cycles, is shown in Fig. 11. The final 1σ bounds are $[\sigma(t_f)]_1 = 5.9\ km$, $[\sigma(t_f)]_2 = 1.2\ km$, $[\sigma(t_f)]_3 = 6.5\ km$, $[\sigma(t_f)]_4 = 0.4\ m/s$, $[\sigma(t_f)]_5 = 0.3\ m/s$, $[\sigma(t_f)]_6 = 0.4\ m/s$. Given that these bounds are sufficiently accurate, the particle filter estimates are suitable for initializing the EKF, which maintains an effective steady state performance.

Extended Kalman Filter for Steady State Operations

The estimation algorithm used after the acquisition of the pulsar integer wavelength from the SSB to the spacecraft is a modified EKF with epoch folding and multirate processing [7]. The dynamical model for this step is Eq. 2. The filter operation can be separated into three time intervals: epoch folding interval, Δt, integration interval, $\Delta\sigma$, and measurement sample interval, $\Delta\tau$. These parameters are essentially tuning parameters, and they are chosen according to the trajectory of the spacecraft. The estimator architecture is shown in Fig. 12. Even though this algorithm was developed
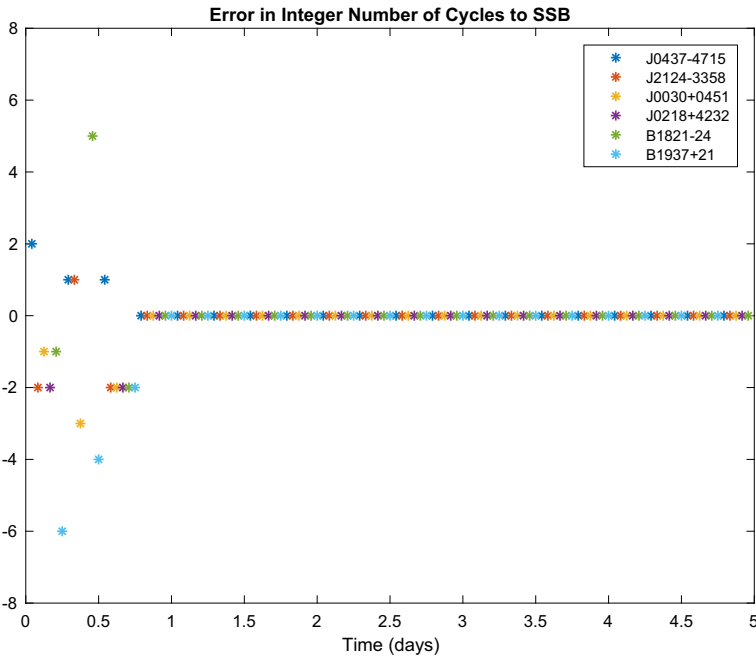
Fig. 11 Error in the number of integer wavelengths to the SSB
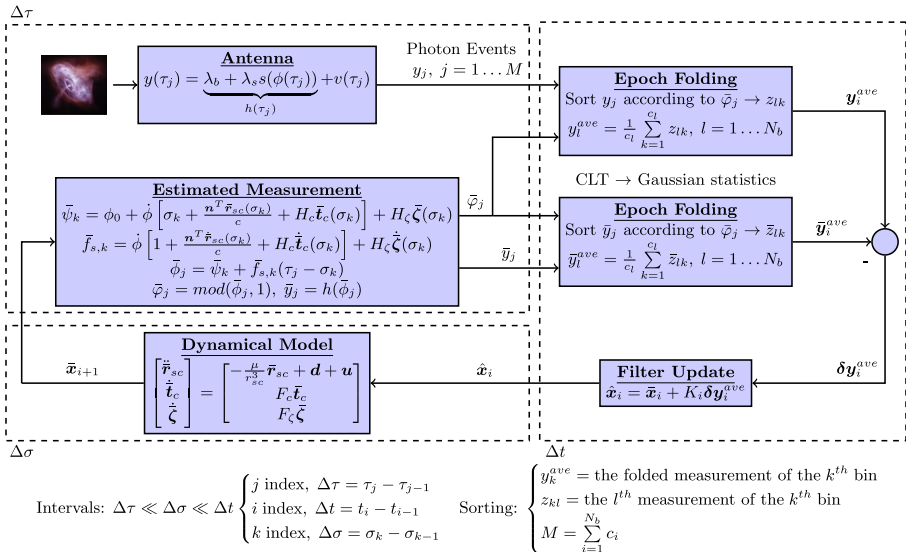

Fig. 12 This block diagram shows an EKF based navigation algorithm with epoch folding [7]. The abbreviation CLT in the figure stands for Central Limit Theorem
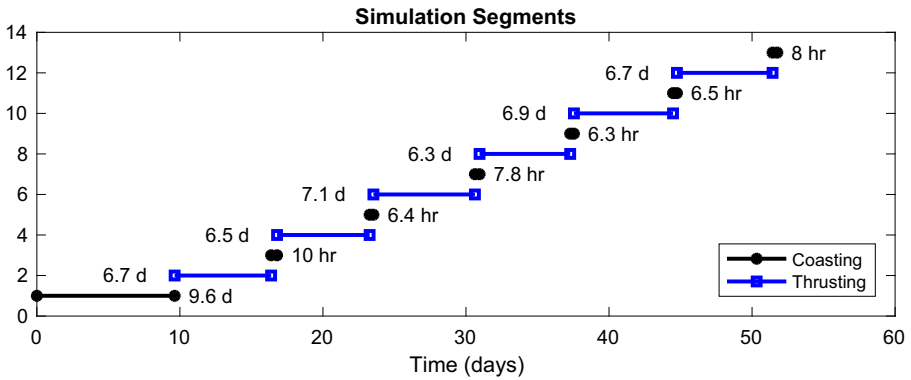
Fig. 13 Thrusting and coasting schedule

for X-ray pulsars, it is also applicable to radio pulsars as long as the first and second moments of the noise process are available.

The dynamics of the pulsar timing noise is a first-order lag with $\omega_c = 1.17 \times 10^{-8}$ and $\alpha = 1$ to simulate the slow varying behavior indicated by Eq. 20. The PSD of the input noise is $W_{\zeta,p} = 9.4 \times 10^{-5}\ s^2/s$. The PSD of the clock process noise is $W_c = \mathrm{diag}[1.6 \times 10^{-21}\ s^2/s,\ 1.0 \times 10^{-32}\ s^2/s^3]$ [23, 38]. The persistent white
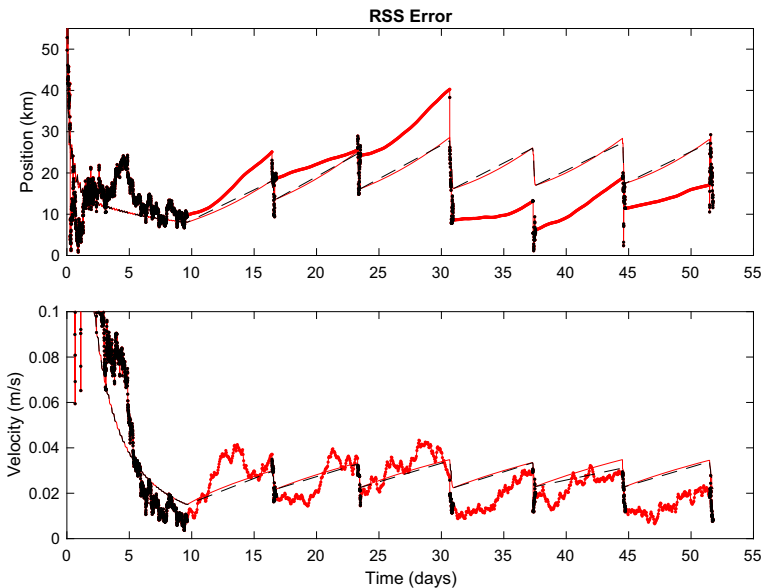

Fig. 14 Red solid and black dashed lines are the *a priori* and a posteriori RSS bounds respectively. The red and black dots are the *a priori* and *a posteriori* RSS estimation errors respectively
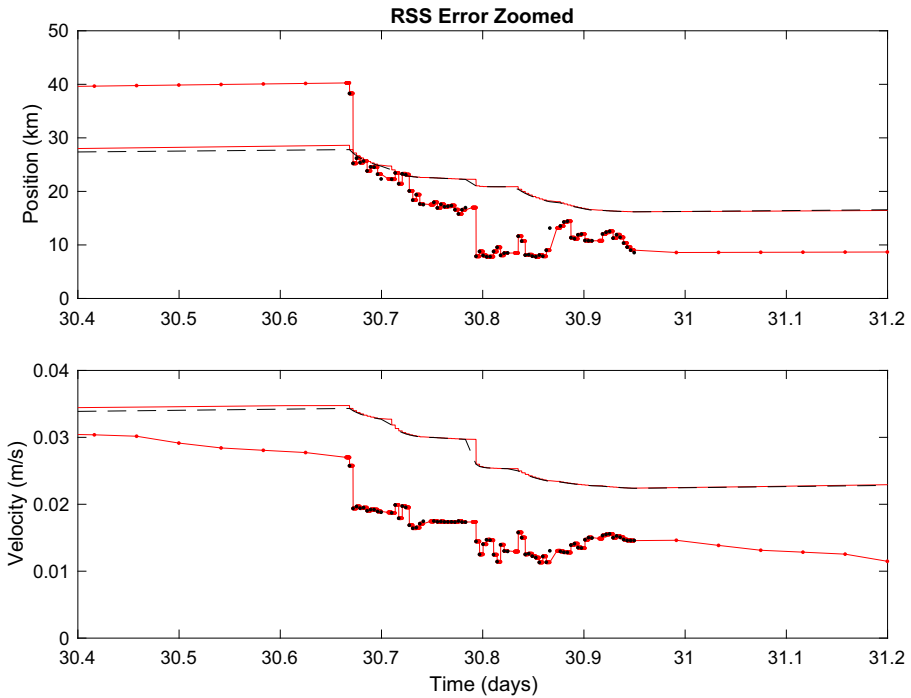
Fig. 15 Zoomed in version of Fig. 14 near day 30

acceleration disturbance has a PSD of $W_r = 3.6 \times 10^{-19} I_{3x3} \ km^2/s^3$. The strength of the ion thruster disturbance, $W_g(t)$, is set according to Eq. 3, where

$$\sigma_{fixed,i} = 10^{-10} \ km/s^2 \text{ for } i = 1, 2, 3$$

$$\sigma_{prop,i} = \begin{cases} 0.25\% & \text{for } i = 1 \\ 4.35 \ mrad & \text{for } i = 2, 3 \end{cases}. \tag{74}$$

Simulation Results

The initial conditions for the true spacecraft position and velocity are randomly generated according to a Gaussian distribution around the values, $\bar{r}_{sc}(t_0)$ and $\dot{\bar{r}}_{sc}(t_0)$, from the Dawn ephemeris. The EKF was initialized using the mean value. The initial error covariance matrix is

$$P(t_0) = \text{diag} \left[P_{r_{sc}}(t_0) \ P_{\dot{r}_{sc}}(t_0) \ P_{t_c}(t_0) \ P_\zeta(t_0) \right], \tag{75}$$

where

$$\begin{aligned} P_{r_{sc}}(t_0) &= 2500 I_{3x3} \ (km^2) \\ P_{\dot{r}_{sc}}(t_0) &= 10^{-6} I_{3x3} \ (km^2/s^2) \\ P_{t_c}(t_0) &= \text{diag}[2.5 \times 10^{-9} \ (s^2), \ 10^{-20} \ (s^2/s^2)] \\ P_\zeta(t_0) &= 2.5 \times 10^{-12} I_{5x5} \ (s^2). \end{aligned} \tag{76}$$

The initial time, t_0, in this scenario is 2454981.66 JED, which is a few days after the Mars gravity assist (2454879.5 JED). Figure 13 shows the simulation segments. The scenario starts with roughly 9.6 days of coasting before the first thrusting segment. A total of 6 thrusting segments and 7 coasting segments are included in this simulation.

It was assumed that the spacecraft is only allowed to observe pulsars during the coasting segments using a single body-mounted detector. Therefore, the spacecraft can only observe one pulsar at a time, and the order of observation is listed in Table 3. After observing the fifth pulsar in the table, the spacecraft returns to observe the first pulsar. The observation time allowed for each pulsar is $T_{obs} = 50\ min$. A time period of 10 min is allocated to slew the spacecraft from one pulsar to another pulsar. The time interval between the ends of two pulsar observations within one coasting segment is $\Delta t = 1\ hr$. The number of pulsar observations within each coasting segment depends on the duration of the coasting segment.

Figures 14 and 15 show the RSS position and velocity estimation errors. After processing pulsar data for 10 days, the RSS position and velocity bounds decrease from 87 km to 8 km and from 1.73 m/s to 0.015 m/s respectively. Because of the high process noise and the lack of measurements during the thrusting segments, the RSS bounds and the estimation errors tend to increase. On average the RSS bounds at the end of each thrusting segment are $\sim 27\ km$ and $\sim 0.03\ m/s$. After approximately 8 hours of observation, the RSS bounds decrease to $\sim 16\ km$ and $\sim 0.02\ m/s$.
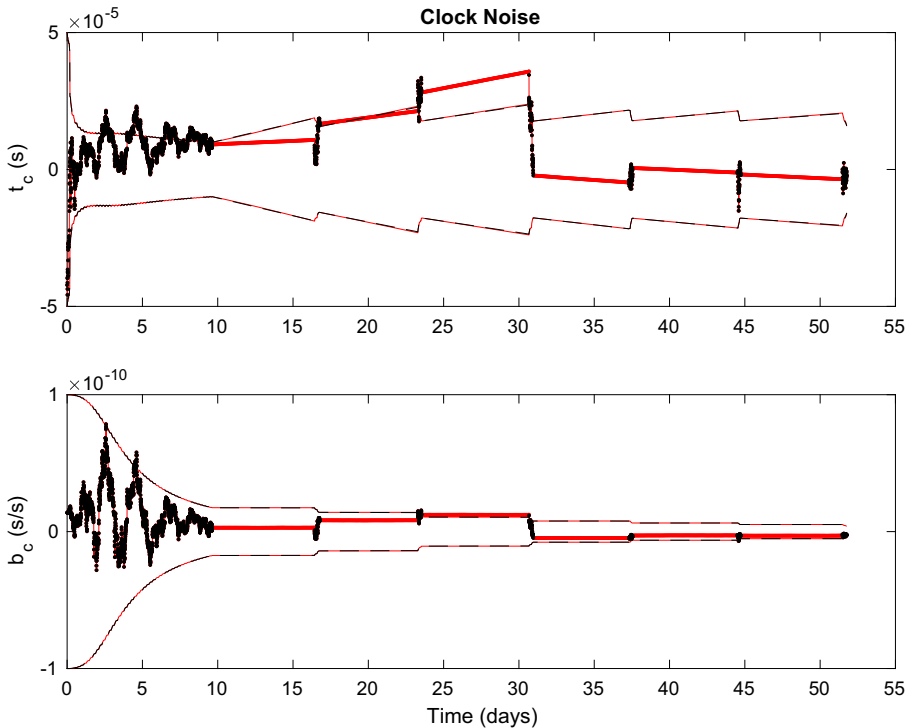

Fig. 16 Estimation errors and 1σ bounds for the two state clock model
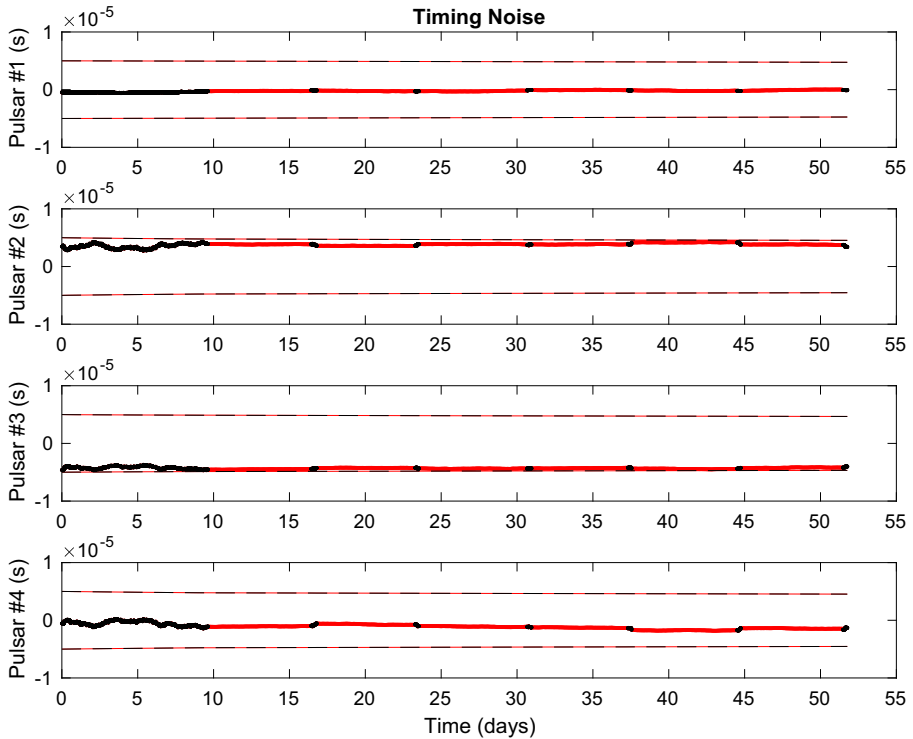
Fig. 17 Estimation errors and 1σ bounds for the pulsar timing noise

These values are consistent with those of Fig. 8, which indicate the integral approximations in the covariance analysis are reasonable. The clock estimation errors are plotted in Fig. 16. Similar behavior occurs in the estimate of the clock bias, $t_c(t)$. This correlation is because both position, $\boldsymbol{r}_{sc}(t)$, and $t_c(t)$ are explicit in the pulsar phase equation, $\phi_{sc}(t)$. The estimation errors for the pulsar correlated noise are shown in Fig. 17. While the 1σ bounds for the pulsar timing noise state are decreasing, they decrease at a slow rate due to the large time constant associated with the pulsar dynamics and the low signal-to-noise ratio pulsar measurements.

Discussion

Equations 34 and 50 are derived using a double integrator system with acceleration input. This simplified system represents a spacecraft on a trajectory composed of segments of constant acceleration and constant velocity. Since the gravitational acceleration due to the Sun in deep space is typically small compared to that experienced by a spacecraft in orbit around a planet, the covariance analysis tool in "Covariance

Analysis" can be used to assess the rough performance of pulsar-based navigation in a deep space mission. The model fidelity can be improved by replacing the double integrator with the linearized dynamics of the inverse squared gravity field along a nominal trajectory. In this case, Eqs. 35 and 41 need be solved numerically. The matrix $Q_p(\Delta t_{k,p}^{obs})$ is also more difficult to compute, because the pulsar signal is no longer periodic. Another approach is to include a lump sum process noise in Eq. 48 to account for the un-modeled dynamics at a cost of using a sub-optimal filter gain.

The set of X-ray and radio pulsars used in the covariance analysis is not optimized. However, it is reasonable to infer from Fig. 8 that a radio-based system with positioning performance on the order of a few tens of kilometers would require an antenna diameter of 11 m. Since a radio antenna can be designed using lightweight materials and be stored in a compact container, it may be possible to use radio pulsar signals for navigation for applications that allow the installation of a large radio antenna. It is noteworthy that we used a conservative receiver bandwidth of 32 MHz from the RadioAstron telescope designed in the 2000s. If the receiver bandwidth can be increased, then the antenna diameter can be reduced to a more manageable size.

Regarding the position acquisition step, it is possible to absorb the function of the signal estimator into the particle filter. For X-ray pulsar navigation, the signal estimator is typically a MLE that processes the X-ray photon time-of-arrivals [10, 35]. Since the particle filter also uses a measurement likelihood function, it is conceptually possible to replace the Gaussian likelihood function with a Poisson likelihood function to simplify the architecture of the position acquisition step.

In order for the particle filter to converge to the true position, it is necessary to have a particle cluster at every integer. A sufficient number of particles is also needed within each cluster to make the filter more resilient against measurement outliers. If the number of particles is not sufficient, then measurement outliers can cause the particle cluster near the true position to disappear through measurement update and particle resampling. The posterior density function before the integer ambiguity is resolved has multiple modes. This can be seen from Fig. 9. Therefore, depending on the distribution of the particles and weights, the estimation error can be much larger than the $3\sigma_{rss, r_{sc}}$ bound as indicated by Fig. 10 at time $t_k = 0.46\ day \approx 11\ hr$. The RSS position error is 7474 km while the RSS bound is 1764 km.

The particle filter was implemented in Matlab and simulated on a laptop equipped with a 2.9 GHz Intel Core i7 processor and 16 GB of memory. The total computation time for a 5 day simulation with 300000 particles was $\sim 1.5\ hr$. The computation aspect of this approach is the main obstacle between theoretical study and a practical implementation. If one were to implement a particle filter for pulsar integer ambiguity resolution, then there is a trade between the size of the initial uncertainty, $P(t_0)$, the measurement update rate, T_{obs}, and the onboard computation resources. Since the individual particle propagation and measurement update are independent from other particles, it is possible to utilize parallel computing to speed up the calculations. We used a relatively basic particle filter and applied a heuristic roughening scheme to the posterior particles based on the geometric properties of the pulsar distribution in the sky. It is possible to refine this approach using more advanced schemes such as a particle filter with adaptive resampling, the auxiliary

particle filter, or the extended Kalman particle filter to more efficiently place the particles in the search region [1, 14].

For the second part of the simulation, an EKF is used to process the pulsar measurements to reduce computation. The advantage of using the EKF for long-term operation is improving the accuracy of the navigation system by incorporating a detailed spacecraft model and time-correlated noise models. Because of the high strength of the ion thruster process noise, $\boldsymbol{w}_g(t)$, and the limited observation time between two thrusting segments, the navigation filter is not able to obtain enough measurements to reach an RSS bound of 8 km as indicated by Fig. 14. This simulation illustrates the importance of the observation duration when there is significant process noise.

Conclusions

In conclusion, this paper investigates the performance of a pulsar-based navigation technique for a spacecraft traveling to deep space using ion thrusters. The result of the covariance analysis is a simple tool that quantifies the rough performance of a pulsar-based navigation system for a given observation schedule, thrusting schedule, and measurement type. However, detailed numerical simulation is still needed to account for other errors such as clock noise and pulsar timing noise. The use of a particle filter allows one to increase the initial uncertainty from 50 km in Cartesian coordinates to 3000 km. This capability improves the robustness of the navigation system against an unforeseen system shutdown. As shown in the numerical simulation that utilizes the Dawn trajectory, if there is no thrusting segment, then the expected root-sum-square position bound is approximately 8 km. If the spacecraft is thrusting, then the position bound oscillates between 27 km and 16 km. The navigation accuracy of the pulsar-based navigation depends on several variables, so it is necessary to perform detailed simulations to explore the trade space of a specific deep space mission.

References

1. Arulampalam, M.S., Maskell, S., Gordon, N., Clapp, T.: A tutorial on particle filters for online nonlinear/non-gaussian bayesian tracking. IEEE Trans. Signal Process. **50**(2), 174–188 (2002). https://doi.org/10.1109/78.978374
2. Bailes, M.: The art of precision pulsar timing. In: Klioner, S.A., Seidelmann, P.K., Soffel, M.H. (eds.) Relativity in fundamental astronomy: Dynamics, reference frames, and data analysis, IAU symposium, vol. 261, pp. 212–217 (2010). https://doi.org/10.1017/S1743921309990421
3. Becker, W., Bernhardt, M.G., Jessner, A.: Autonomous spacecraft navigation with pulsars. https://doi.org/10.2420/AF07.2013.11 (2013)
4. Bregni, S.: Synchronization of digital telecommunications networks, vol. 27. Wiley, New York (2002). https://doi.org/10.1002/0470845880.ch4

5. Campbell, D.B.: Measurement in radio astronomy. In: Stanimirovic, S., Altschuler, D., Goldsmith, P., Salter, C. (eds.) Single-dish radio astronomy: Techniques and applications, astronomical society of the pacific conference series, vol. 278, pp. 81–90 (2002)

6. Charef, A., Sun, H., Tsao, Y., Onaral, B.: Fractal System as Represented by Singularity Function. IEEE Trans. Autom. Control **37**(9), 1465–1470 (1992). https://doi.org/10.1109/9.159595

7. Chen, P.T., Speyer, J.L., Bayard, D.S., Majid, W.A.: Autonomous navigation using x-ray pulsars and multirate processing. J. Guid. Control Dynam. **40**(9), 2237–2249 (2017). https://doi.org/10.2514/1.G002705

8. Coles, W., Hobbs, G., Champion, D., Manchester, R., Verbiest, J.: Pulsar Timing Analysis in the Presence of Correlated Noise. Mon. Not. R. Astron. Soc. **418**(1), 561–570 (2011). https://doi.org/10.1111/j.1365-2966.2011.19505.x

9. Edwards, R., Hobbs, G., Manchester, R.: TEMPO2, A new pulsar timing package–II. The Timing Model and Precision Estimates. Mon. Not. R. Astron. Soc. **372**(4), 1549–1574 (2006). https://doi.org/10.1111/j.1365-2966.2006.10870.x

10. Emadzadeh, A.A., Speyer, J.L.: Navigation in space by x-ray pulsars. Springer, New York (2011). https://doi.org/10.1007/978-1-4419-8017-5

11. Gates, C.R.: A simplified model of midcourse maneuver execution errors. Tech Rep. 32-504, Jet Propulsion Laboratory, California Institute of Technology (1963)

12. Golshan, A.R., Sheikh, S.I.: On pulse phase estimation and tracking of variable celestial x-ray sources. In: Proceedings of the 63rd annual meeting of the institute of navigation, pp. 413–422 (2001)

13. Hobbs, G., Edwards, R., Manchester, R.: TEMPO2, a new pulsar-timing package–i. an overview. Mon. Not. R. Astron. Soc. **369**(2), 655–672 (2006). https://doi.org/10.1111/j.1365-2966.2006.10302.x

14. Hwang, S.S., Speyer, J.L.: Particle filters with adaptive resampling technique applied to relative positioning using GPS carrier-phase measurements. IEEE Trans. Control Syst. Technol. **19**(6), 1384–1396 (2010). https://doi.org/10.1109/TCST.2010.2091415

15. Irwin, A.W., Fukushima, T.: A Numerical Time Ephemeris of the Earth. Astron. Astrophys. **348**, 642–652 (1999)

16. Jodrell Bank Observatory: The European Pulsar Network Data Archive. [Online Database]. http://www.jb.man.ac.uk/pulsar/Resources/epn/

17. Kardashev, N., Kovalev, Y., Kellermann, K.: Radioastron: An earth-space radio interferometer with a 350,000 km baseline. URSI Radio Sci. Bull. **2012**(343), 22–29 (2012)

18. Liu, J., Ma, J., Tian, J., Kang, Z., White, P.: Pulsar navigation for interplanetary missions using CV model and ASUKF. Aerosp. Sci. Technol. **22**(1), 19–23 (2012)

19. Lorimer, D.R., Kramer, M.: Handbook of pulsar astronomy, vol. 4. Cambridge University Press, Cambridge (2005)

20. Manchester, R., Hobbs, G., Teoh, A., Hobbs, M.: The Australia telescope national facility pulsar catalogue. The Astronomical Journal **129**(4), 1993 (2005)

21. Mitchell, J.W., Winternitz, L.M., Hassouneh, M.A., Price, S.R., Semper, S.R., Yu, W.H., Ray, P.S., Wolff, M.T., Kerr, M., Wood, K.S., et al.: Sextant x-ray pulsar navigation demonstration: Initial on-orbit results. In: Proceedings of the advances in the astronautical sciences guidance, navigation and control 2018, vol. 164 (2018)

22. NASA: Planetary and lunar ephemerides. [Online Database] (2015). http://ssd.jpl.nasa.gov/?ephemerides

23. Oaks, O.J., McCaskill, T.B., Largay, M.M., Reid, W.G., Buisson, J.A.: Performance of GPS on-orbit NAVSTAR frequency standards and monitor station time references. In: Proceedings of the 30th annual precise time and time interval (PTTI) meeting (1998)

24. Ray, P., Wood, K., Phlips, B.: Spacecraft Navigation Using X-Ray Pulsars. Tech. Rep., Naval Research Laboratory, E. O. Hulburt Center for Space Research (2006)

25. Rayman, M.D., Mase, R.A.: Dawn's operations in cruise from vesta to ceres. Acta Astronautica **103**, 113–118 (2014). https://doi.org/10.1016/j.actaastro.2014.06.042. http://www.sciencedirect.com/science/article/pii/S0094576514002410

26. Reardon, D., Hobbs, G., Coles, W., Levin, Y., Keith, M., Bailes, M., Bhat, N., Burke-Spolaor, S., Dai, S., Kerr, M., et al.: Timing analysis for 20 millisecond pulsars in the parkes pulsar timing array. Mon. Not. R. Astron. Soc. **455**(2), 1751–1769 (2015). https://doi.org/10.1093/mnras/stv2395

27. Russell, C., Raymond, C.: The dawn mission to minor planets 4 vesta and 1 ceres. Springer Science & Business Media. https://doi.org/10.1007/978-1-4614-4903-4 (2012)

28. Sala, J., Urruela, A., Villares, X., Estalella, R., Paredes, J.M.: Feasibility study for a spacecraft navigation system relying on pulsar timing information. ARIADNA Study **3**(4202.2003), 6 (2004)

29. Sheikh, S.I., Hanson, J.E., Graven, P.H., Pines, D.J.: Spacecraft navigation and timing using x-ray pulsars. Navigation **58**(2), 165–186 (2011). https://doi.org/10.2514/1.13331

30. Sheikh, S.I., Pines, D.J.: Recursive estimation of spacecraft position using x-ray pulsar time of arrival measurements. In: ION 61st annual meeting, pp. 464–475 (2005). https://doi.org/10.1002/j.2161-4296.2006.tb00380.x

31. Simon, D.: Optimal state estimation: Kalman, H-Infinity, and nonlinear approaches. John Wiley & Sons. https://doi.org/10.1002/0470045345 (2006)

32. Speyer, J.L., Chung, W.H.: Stochastic processes, estimation, and control, vol. 17. Siam. https://doi.org/10.1137/1.9780898718591 (2008)

33. Wei, E., Jin, S., Zhang, Q., Liu, J., Li, X., Yan, W.: Autonomous navigation of mars probe using x-ray pulsars: Modeling and results. Adv. Space Res. **51**(5), 849–857 (2013). https://doi.org/10.1016/j.asr.2012.10.009

34. Winternitz, L.M., Hassouneh, M.A., Mitchell, J.W., Valdez, J.E., Price, S.R., Semper, S.R., Wayne, H.Y., Ray, P.S., Wood, K.S., Arzoumanian, Z., et al.: X-ray pulsar navigation algorithms and testbed for SEXTANT. In: 2015 IEEE aerospace conference, pp. 1–14. IEEE (2015). https://doi.org/10.1109/AERO.2015.7118936

35. Winternitz, L.M., Mitchell, J.W., Hassouneh, M.A., Valdez, J.E., Price, S.R., Semper, S.R., Wayne, H.Y., Ray, P.S., Wood, K.S., Arzoumanian, Z., et al.: SEXTANT x-ray pulsar navigation demonstration: Flight system and test results. In: Aerospace conference, 2016 IEEE, pp. 1–11. IEEE (2016). https://doi.org/10.1109/AERO.2016.7500838

36. Wolfe, J.D., Speyer, J.L., Lee, E., Lee, Y.J., Hwang, S.: Estimation of relative satellite position using transformed differential carrier-phase GPS measurements. J. Guid. Control Dynam. **30**(5), 1217–1227 (2007). https://doi.org/10.2514/1.11691

37. Wolfe, J.D., Williamson, W.R., Speyer, J.L.: Hypothesis testing for resolving integer ambiguity in GPS. Navigation **50**(1), 45–56 (2003). https://doi.org/10.1002/j.2161-4296.2003.tb00317.x

38. Wright, J.R.: GPS composite clock analysis. International Journal of Navigation and Observation. https://doi.org/10.1155/2008/261384 (2008)